



A mean-line model to predict the design efficiency of radial inflow turbines in organic Rankine cycle (ORC) systems



Luca Da Lio, Giovanni Manente*, Andrea Lazzaretto

University of Padova, Department of Industrial Engineering, via Venezia 1, 35131 Padova, Italy

HIGHLIGHTS

- A mean-line model of radial inflow turbines in ORC systems is developed.
- The model includes a novel design and performance analysis procedure.
- Optimum values of specific speed and velocity ratio are obtained.
- The influence of the size and expansion ratio on the design efficiency is evaluated.

ARTICLE INFO

Keywords:

Organic Rankine cycle
Radial inflow turbine
Efficiency maps
Aungier's loss correlations
Size parameter
Volumetric expansion ratio

ABSTRACT

Organic Rankine Cycle (ORC) systems represent an efficient technology for power generation from low-to-medium temperature heat sources. Most of the efforts in the recent literature are addressed to the improvement of turbine design and efficiency by taking advantage of the low enthalpy drops while dealing with the large volume flow ratios across the expansion process and low speed of sound typical of high molecular weight fluids. These peculiar conditions make the choice and the design of an ORC turbine a challenging task, exacerbated by the only few experimental data available in the open literature. The aim of this paper is to obtain the optimum design and corresponding maximum efficiency of single stage radial inflow turbines for different cycle design specifications (i.e., mass flow rate and enthalpy drop) using the real gas properties of refrigerant R245fa. This aim is pursued by means of a mean-line model developed in Matlab® which includes the design and performance analysis procedure suggested by Aungier (2005). Results indicate how different design choices in terms of specific speed and velocity ratio, and different working conditions in terms of expansion ratio and turbine size may affect the efficiency of single stage radial inflow turbines in ORC systems.

1. Introduction

Turbine efficiency in organic Rankine cycle (ORC) systems basically depends on the turbine configuration (axial, radial inflow, radial outflow), design choices (loading and flow coefficients, degree of reaction, specific speed, velocity ratio, etc.), operating conditions (inlet pressure, inlet temperature, outlet pressure, mass flow rate) and working fluid. The results of optimization studies of ORC systems in the literature show that the power output increases only marginally when choosing among the best fluids. However, this performance gap may increase when taking into account turbine efficiency. Thus, an accurate evaluation of turbine performance may dictate the final choice of the ORC design.

Pan et al. [1] warn against the use of a constant isentropic efficiency, which may lead to a misleading selection of the optimum

working fluid and cycle parameters. Bahamonde et al. [2] presented a new method for the optimum preliminary design of the turbine performed simultaneously with the optimum design of the ORC system. They showed that the highest ORC system efficiency is obtained by a RIT configuration, whereas lower efficiencies are achieved by three stage axial and radial outflow designs. Casati et al. [3] presented a novel design methodology for radial outflow turbines operating in high temperature mini-ORCs (10 kW_e). The authors explained that this turbine configuration benefits from the natural increase of the passage area along the flow path, in accordance with the increase in volumetric flow rate.

While multistage axial and radial outflow configurations may represent suitable design options, the radial inflow design can achieve comparable efficiencies at lower costs. Nonetheless, the selection of proper design parameters is critical in the search of high efficiencies as

* Corresponding author.

E-mail address: giovanni.manente@unipd.it (G. Manente).

Nomenclature**Abbreviations**

<i>LPT</i>	low pressure turbine
<i>ORC</i>	organic Rankine cycle
<i>RIT</i>	radial inflow turbine

Variables

<i>a</i>	speed of sound, m/s
<i>A</i>	passage area, m ²
<i>b</i>	blade height or passage width, m
<i>C</i>	absolute velocity, m/s
<i>c</i>	chord, m
<i>c_f</i>	skin friction coefficient
<i>C₀</i>	spouting velocity, m/s
<i>D</i>	diameter, m
<i>esse</i>	blade pitch, m
<i>h</i>	specific enthalpy, kJ/kg
<i>I</i>	rothalpy, kJ/kg
<i>i</i>	incidence angle, °
<i>k_b</i>	blockage factor
<i>k_{load}</i>	blade loading
<i>L</i>	flow path length, m
<i>M</i>	Mach number
<i>n</i>	rotational speed, rpm
<i>n_s</i>	specific speed
<i>N</i>	number of blades
<i>m</i>	mass flow rate, kg/s
<i>o</i>	throat width, m
<i>p</i>	pressure, bar or kPa
<i>r</i>	radius, m
<i>R</i>	degree of reaction
<i>R_C</i>	radius of curvature of the meridional channel, m
<i>s</i>	specific entropy, kJ/kg-K
<i>SP</i>	size parameter (m)
<i>t</i>	blade thickness, m
<i>T</i>	temperature, °C
<i>U</i>	peripheral speed, m/s
<i>V̇</i>	volumetric flow rate, m ³ /s
<i>VR</i>	volumetric expansion ratio
<i>W</i>	relative velocity, m/s
<i>Y</i>	total pressure loss coefficient

Greek symbols

α	flow angle, °
β	blade angle, °
Δ	normalized mass defect thickness
δ_c	clearance gap, m
Δ_w	wall boundary layer blockage
δ_w^*	displacement thickness, m
Δz	axial length, m
ϵ	convergence tolerance
γ	setting angle, °

ϕ	flow coefficient, curvature
ψ	loading coefficient
v_s	velocity ratio
η_s	total-to-static efficiency, %
κ_m	mean curvature of the meridional channel
ρ	density, kg/m ³
θ	blade camberline angle, °
Θ	normalized momentum defect thickness
ω	angular velocity, rad/s

Subscripts

0	total state
1	volute inlet (design routine), inlet station (performance routine)
2	nozzle inlet (design routine), mid station (performance routine)
3	nozzle outlet (design routine), outlet station (performance routine)
4	rotor inlet (design routine)
5	rotor outlet (design routine)
<i>a</i>	annulus
<i>ave</i>	average
<i>b</i>	blade
<i>bl</i>	blade loading
<i>bp</i>	blade pressure
<i>bs</i>	blade suction
<i>cl</i>	clearance
<i>df</i>	disk friction
<i>dis</i>	discharge
<i>e</i>	electrical
<i>evap</i>	evaporating
<i>ex</i>	post-expansion
<i>h</i>	hub
<i>hs</i>	hub-to-shroud
<i>in</i>	inlet
<i>inc</i>	incidence
<i>m</i>	meridional or mean
<i>max</i>	maximum
<i>min</i>	minimum
<i>n</i>	nozzle
<i>out</i>	outlet
<i>p</i>	profile
<i>r</i>	rotor
<i>R</i>	relative
<i>s</i>	shroud or isentropic
<i>t</i>	tangential
<i>tot</i>	total
<i>v</i>	volute
<i>w</i>	wall

Superscripts

'	relative frame
*	sonic or ideal flow conditions

highlighted by Ventura et al. [4], who explored a large spectrum of flow coefficients (ϕ), loading coefficients (ψ) and rotational speeds (n). Although their model relies on the ideal gas assumption, still it gives some useful indications for the design of RIT in ORC systems. Wong et al. [5] explored the feasibility of using the similarity concepts to estimate the performance of a RIT for two refrigerants (R134a and R245fa) by scaling performance data available for air. Different approaches based

on similarity concepts were investigated. The simplest one, which assumes an ideal gas behavior, provided the largest error. Instead, the “variable pressure ratio approach”, which guarantees the dynamic similarity, provided the highest accuracy.

While the application of design guidelines originally developed for common gases (air, flue gases) may be useful to start the design, meanline models specifically developed for organic fluids taking into account

their real gas behavior are needed. To this purpose, Fiaschi et al. [6] developed a mean-line model of a RIT for a 50 kW_e ORC system considering six working fluids. In a subsequent study [7] the same authors carried out a parametric analysis to assess losses against the main design parameters, namely ϕ , ψ and the degree of reaction (R). Song et al. [8] presented a one-dimensional analysis model of a medium size (250 kW_e) RIT for ORC systems using a heat source at 120 °C and considering seven working fluids with critical temperatures in the range 125–205 °C. The optimum working fluid changed (from R236fa to R236ea) when turbine efficiency was taken into account, unlike conventional analyses which set the turbine efficiency at a constant value for all fluids. Rahbar et al. [9] developed a methodology for the optimization of a 15 kW_e radial turbine for ORC applications considering eight working fluids and turbine inlet temperatures in the range 60–145 °C. The authors employed a genetic algorithm to maximize η_s by varying ψ and ϕ in the range 0.6–1.4 and 0.2–0.5, respectively, and the rotational speed between 35,000 and 65,000 rev/min. The maximum η_s was found to vary between 82.9% and 84.0%. The optimum values of n_s and v_s were close to 0.42 and 0.62, respectively. Lang et al. [10] carried out a study on an ORC system which recovers waste heat from an heavy-duty truck engine. The authors designed the expander following the procedure described by Whitfield and Baines [11], though it is strictly valid only for subsonic RIT. Costall et al. [12] compared toluene and a linear siloxane (MDM) as working fluids in a small scale ORC RIT used to recover waste heat at 300 °C from a 360 kW_e Diesel engine. Unlike common design guidelines, which suggest a limiting value of the outlet shroud radius to rotor inlet radius ratio equal to 0.6–0.7, they imposed a limiting value of 0.95 which appears excessive to ensure stable flow conditions inside the rotor.

Recently, many studies have appeared in the literature which either confirm or revise the turbine efficiency predictions obtained by the mean-line analyses by performing CFD simulations. For instance, Fiaschi et al. [13] recently developed a design procedure for a micro radial ORC turbine (5 kW_e) made up of a mean-line model for the preliminary sizing, further refined by a 3D approach to maximize the performance. Sauret et al. [14] carried out a preliminary mean-line design and 3D CFD simulation of a 400 kW_e radial inflow turbine for a geothermal supercritical ORC system using R143a as working fluid. The preliminary design was performed using the commercial software RITAL[®], which embeds the design procedure described by Moustapha et al. in [15]. The flow and loading coefficients were set to 0.215 and 0.918, respectively, which should give the highest turbine efficiency according to the chart proposed by Baines [16]. The resulting η_s predicted by RITAL[®] was quite low (76.8%). However, the results of the 3D CFD simulations provided a much higher efficiency (83.5%), which may raise doubts about the accuracy of mean-line models in predicting a proper efficiency. Zheng et al. [17] investigated the design and off-design performance of a 640 kW_e RIT using R134a as working fluid. Similarly to Sauret et al. [14], the CFD simulation carried out using the commercial software ANSYS-CFX[®] provided a comparatively higher η_s (equal to 84.3%) compared to the mean-line analysis. Li et al. [18] carried out an aerodynamic design of a RIT operating in a half MW_e ORC system using R123 as working fluid and fed by a waste heat source at 180 °C. The one-dimensional aerodynamic design provided a turbine efficiency of 84.3% whereas the application of the 3D numerical model resulted in a higher turbine efficiency (85.79%). Dong et al. [19] carried out an aerodynamic design of a 170 kW_e radial turbine used in a high temperature supercritical ORC system. Due to the high pressure ratio in the expansion process (37.3) they opted for a two-stage radial turbine. Al Jubori et al. [20] presented a new integrated approach which combines ORC system modeling, mean-line design and 3D CFD analysis for micro-scale RIT generating a power output of a few kW_e. They focused on five organic working fluids (R1234yf, R141b, R245fa, n-butane and n-pentane) for utilization of low grade heat sources. Unlike the above-mentioned studies, the total-to-total turbine efficiencies predicted by the mean line model (85–86%) were approximately 3.0%–

points higher compared to those obtained by the 3D CFD analysis. Based on CFD simulations the authors showed that the efficiency of radial inflow turbines is higher compared to micro-scale axial turbines at pressure ratios higher than 3.0.

Although the comparison with the 3D CFD simulation can be useful to check the efficiency predicted by the mean-line models, a true validation can be performed only through experimentations. However, there are only few experimental studies on ORC systems equipped with RIT. Kang [21] designed and tested a 30 kW_e RIT having an inlet temperature of 80 °C and using R245fa as working fluid. The turbine was designed based on the geometrical similarity with a model turbine and using air as working fluid. They obtained a maximum η_s of 78.7%. In a following study [22] the same author designed a two-stage RIT for utilization of a higher temperature heat source. Guillaume et al. [23] carried out an experimental campaign to evaluate the performance of a micro scale ORC system (3.5 kW_e) equipped with a RIT to recover waste heat from a truck engine. They compared two working fluids: R245fa and its substitute R1233zd, having a much lower GWP. The turbine was developed using components of truck turbochargers and showed efficiencies in the range 60–75%. In summary, it can be observed that the measured turbine efficiencies are generally lower than expected mainly because the tested turbines were not specifically designed for high molecular weight fluids, but rather adapted from the operation with air [21,22] or exhaust gases [23].

In this paper a mean-line model to design and predict the efficiency of RITs operating with R245fa is developed. Unique in the literature, the model includes the preliminary design and performance analysis procedure proposed by Aungier [24]. This procedure includes general loss correlations, which are suitable for analyzing a wide spectrum of turbine sizes and working conditions. For instance, the profile losses are evaluated referring to the general boundary layer analysis, rather than using correlations based on empirical constants of limited applicability. Moreover, besides the inlet and outlet stations also a mid-station is added within each turbine component (volute, nozzle, rotor) to refine the performance prediction.

The predicted turbine efficiencies are presented in two classes of maps: the first correlates the total-to-static efficiency with the turbine designer choices (namely n_s and v_s) at given working conditions; the second correlates the total-to-static efficiency with the working conditions considering only optimum turbine designer choices (i.e., optimum n_s and v_s). Working conditions are expressed in terms of size parameter (SP) and volumetric expansion ratio (VR) which, unlike the rotor diameter and pressure ratio, already include in their definition the fluid properties. Consequently, the maps obtained in this work for R245fa can be considered general and roughly applicable to any fluid, as explained in [25,26]. These new maps update and extend those developed in the late eighties by Perdichizzi and Lozza [27], where the most accurate loss correlations available at that time and the simplified hypothesis of an ideal gas behavior of the organic fluid were adopted.

The obtained efficiency maps give useful guidelines for the optimum selection of the design parameters and provide an accurate evaluation of the maximum turbine efficiency for a variety of working conditions. These maps can be easily embedded in an overall optimization procedure of the ORC system, as recently shown by authors in [28,29], which finally dictates the optimum turbine choice.

2. Methodology

An original in-house code was developed by the authors in the Matlab[®] environment to carry out the design and performance prediction of the radial inflow turbine, using Refprop[®] [30] to calculate accurate fluid properties for R245fa. Fig. 1 shows the global code architecture, which is composed of two main routines, namely the “design routine” and the “performance routine” (in bold in Fig. 1). The design routine determines the RIT geometry starting from the specifications dictated by the thermodynamic analysis, the designer choices on

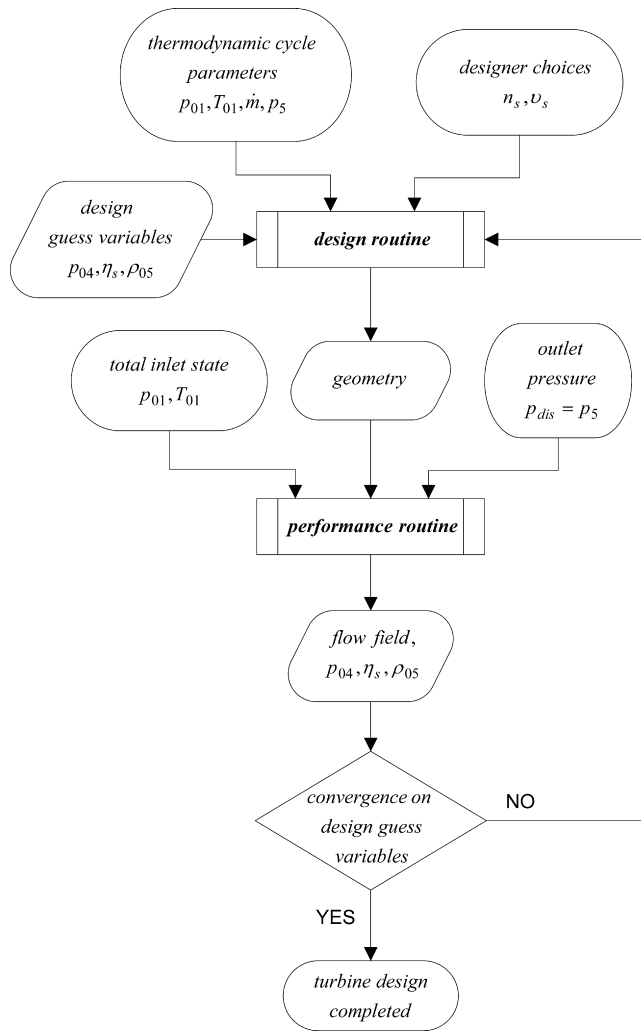


Fig. 1. General model architecture for the design and performance analysis of a radial inflow turbine.

specific speed and velocity ratio and some first guess values to initialize the calculations. Instead, the performance routine evaluates the flow field in the RIT and the resulting efficiency using the geometry and the total inlet state and discharge pressure as inputs. The final design of a RIT requires several cascaded runs of the design and performance routines, to update the guess values used in the design, till convergence.

In the following Sections the design and performance routines are presented, also using detailed flowcharts which graphically show the equations, the main assumptions and the calculation procedure. In particular, Section 2.1 is about the design of the expander components, whereas Section 2.2 is about the performance prediction. In the last part of Section 2.2, some hints are given to manage two specific issues which were solved using several iterative loops and blocks of instructions.

2.1. Design routine

As shown in Fig. 1 the input data for the design routine are: (i) the turbine inlet state (p_{01} , T_{01}), the turbine outlet pressure (p_5) and the mass flow rate of the working fluid (\dot{m}), given by the thermodynamic analysis; (ii) the couple specific speed (n_s) – velocity ratio (v_s); (iii) first guess values for some variables (total-to-static efficiency η_s , total pressure at rotor inlet p_{04} , total density at rotor outlet ρ_{05}) and (iv) some kinematic/geometrical assumptions (e.g., null tangential velocity at rotor outlet, blade thickness, etc.). Fig. 2 depicts the meridional view of the inflow radial turbine and the nozzle showing the relevant

geometrical parameters using the notation employed in the design routine.

2.1.1. Rotor inlet

The various steps in the design of the rotor inlet station are outlined in Fig. 3. The combined choice of specific speed (n_s) and velocity ratio (v_s) gives the rotational speed (n) and turbine diameter (D_4). The Euler equation provides the tangential absolute velocity at rotor inlet (C_{t4}) required to achieve the desired specific work assuming a zero swirl at turbine exit ($C_{t5} = 0$). The absolute angle at rotor inlet (α_4) is estimated by a correlation with n_s predicting higher flow angles at higher n_s values. Accordingly, the meridional velocity (C_{m4}), relative velocity (W_4) and the overall velocity triangle at turbine inlet can be calculated. The static enthalpy at rotor inlet (h_4) can be directly calculated from the total enthalpy, which is constant in the stator (i.e., $h_{01} = h_{04}$), and the absolute velocity (C_4). By combining the information on h_4 and p_{04} (a guess variable at the beginning of the design), the thermodynamic state at rotor inlet is fully defined. The flow angle α_4 is also used to evaluate the optimum number of rotor blades (N_r) by using a correlation available in [24], which gives a higher number of blades at lower α_4 . The rotor inlet blade height (b_4) directly derives from the continuity equation, taking into account the inlet metal blockage factor (k_{b4}), which needs an assumption on the blade thickness (t_{b4}).

2.1.2. Rotor outlet

The steps in the design of the rotor outlet station and the meridional channel are shown in the flowchart of Fig. 4.

Preliminary design of the rotor outlet station

The design starts from the basic assumptions of a nearly constant meridional velocity throughout the rotor and zero exit swirl. From the guess value of turbine efficiency (η_s), the total enthalpy at rotor outlet

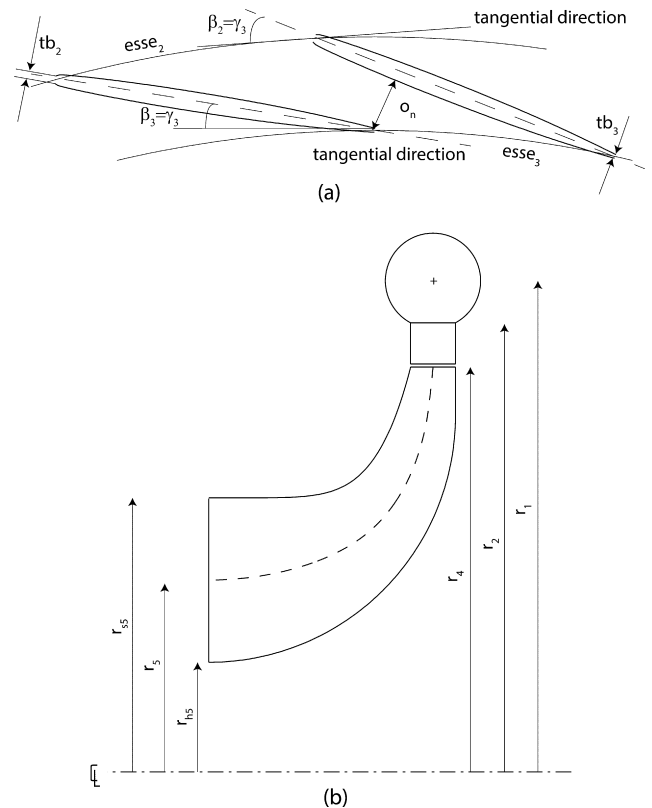


Fig. 2. Radial inflow turbine: (a) Nozzle geometry; (b) Meridional view of the radial inflow turbine.

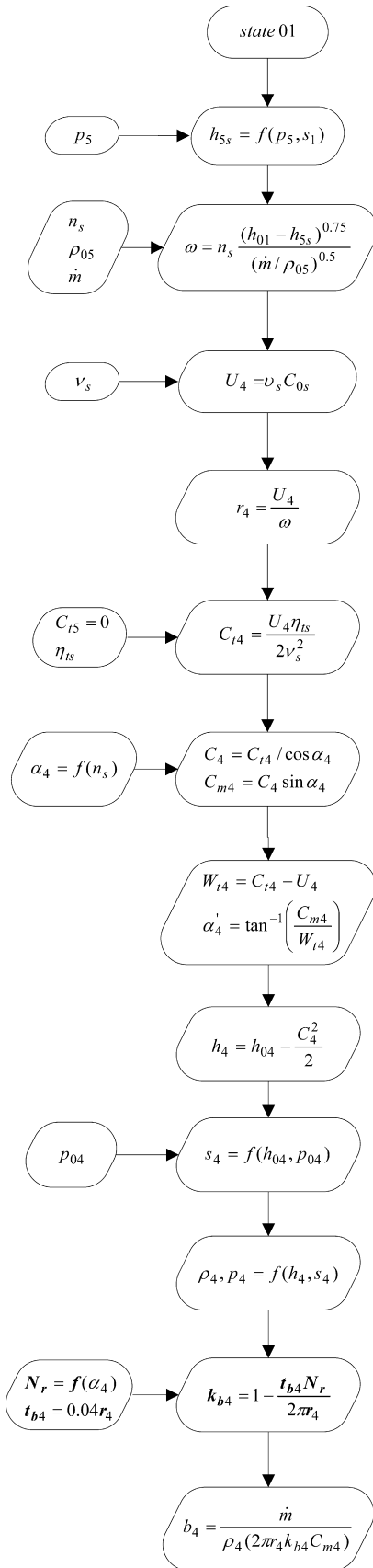


Fig. 3. Design of the rotor inlet.

can be calculated and, in turn, the static enthalpy (h_5). So, all the thermodynamic variables at rotor exit can be calculated, being the discharge pressure (p_5) a design specification. The exit hub radius (r_{h5}) is simply estimated as a percentage of the rotor inlet radius, whereas the exit shroud radius (r_{s5}), which is obtained by the continuity equation, requires an iterative mass balance to converge on the outlet blockage factor (k_{b5}). By simply calculating the rotor exit radius (r_5) as mathematical average of the hub and shroud radii, the velocity triangle at rotor exit is fully defined. In case the blockage at rotor exit is too high (i.e., $k_{b5} < 0.50$), the number of blades is progressively reduced and all variables depending on N_r must be consequently recalculated.

Geometrical constraints

The geometry of the rotor outlet must fulfill the two main constraints (see, e.g., [11,24]) related to the maximum shroud radius, in order to avoid an excessive curvature of the meridional channel ($r_{s5} < 0.7r_4$), and the minimum hub radius for the shaft ($r_{h5} > 0.4r_{s5}$). A third constraint ($A_5/A_4 < 2.5$) is added in this study to limit the significant increase of the flow passage area from turbine inlet to outlet dictated by the high density variation. In fact, this may cause flow separation and the generation of span-wise velocity components, which can be detected only by a detailed 3D CFD study. All these constraints (Table 1) concur to the reduction of the flow discharge passage area and, in turn, to the increase of the meridional velocity at rotor outlet (C_{m5}). This adjustment causes an increase of the relative flow angle which sets the blade angle (β_5) at rotor exit. As the overriding majority of turbine designs considered in this study shows subsonic relative flow conditions at rotor outlet, the rotor throat width (o_5) can be directly evaluated from the blade pitch ($esse_5$) by continuity between throat and exit sections. Instead, if supersonic flow conditions occur, further calculations are needed, as shown in upper right blocks in Fig. 4. Finally, the axial length of the rotor (Δz_r) is directly obtained from the blade height at rotor outlet.

Design of the meridional channel

The rotor hub contour is designed to minimize passage curvature effects by using the largest circular-arc that is compatible with the rotor dimensions previously obtained. A power-law relation parametric with ξ (see paragraph 10.6 in [24]) allows the definition of the shroud contour in order to achieve a passage area on the mean quasi-normal (A_m) that is approximately equal to the average of the rotor inlet and outlet passage areas. Straight-line element blades are adopted. Blade angle distributions (β) along the meridional coordinate for hub, shroud and mid-line can be calculated from the corresponding camberline blade angle distributions (θ).

2.1.3. Nozzle

Fig. 5 shows in detail all the calculations required to design the nozzle, which are summarized in the following.

Number of nozzle blades

The passage width is assumed constant throughout the nozzle and equal to the blade height at rotor inlet. The tangential absolute velocity at nozzle outlet (C_{t3}) is simply obtained by the conservation of the angular momentum in the annulus. As the blade loading criterion ($k_{load} = 1$), which determines the optimum number of nozzle blades (N_n), involves variables which will be known only at the end of the design procedure, it is necessary to repeat the design procedure for a set of nozzles having different N_n (in the range 18–33). Moreover, guess values for blade blockage (k_{b3}), fluid density (ρ_3) and blade setting angle (γ_3) are required to initialize the calculations and updated until convergence (see Fig. 5).

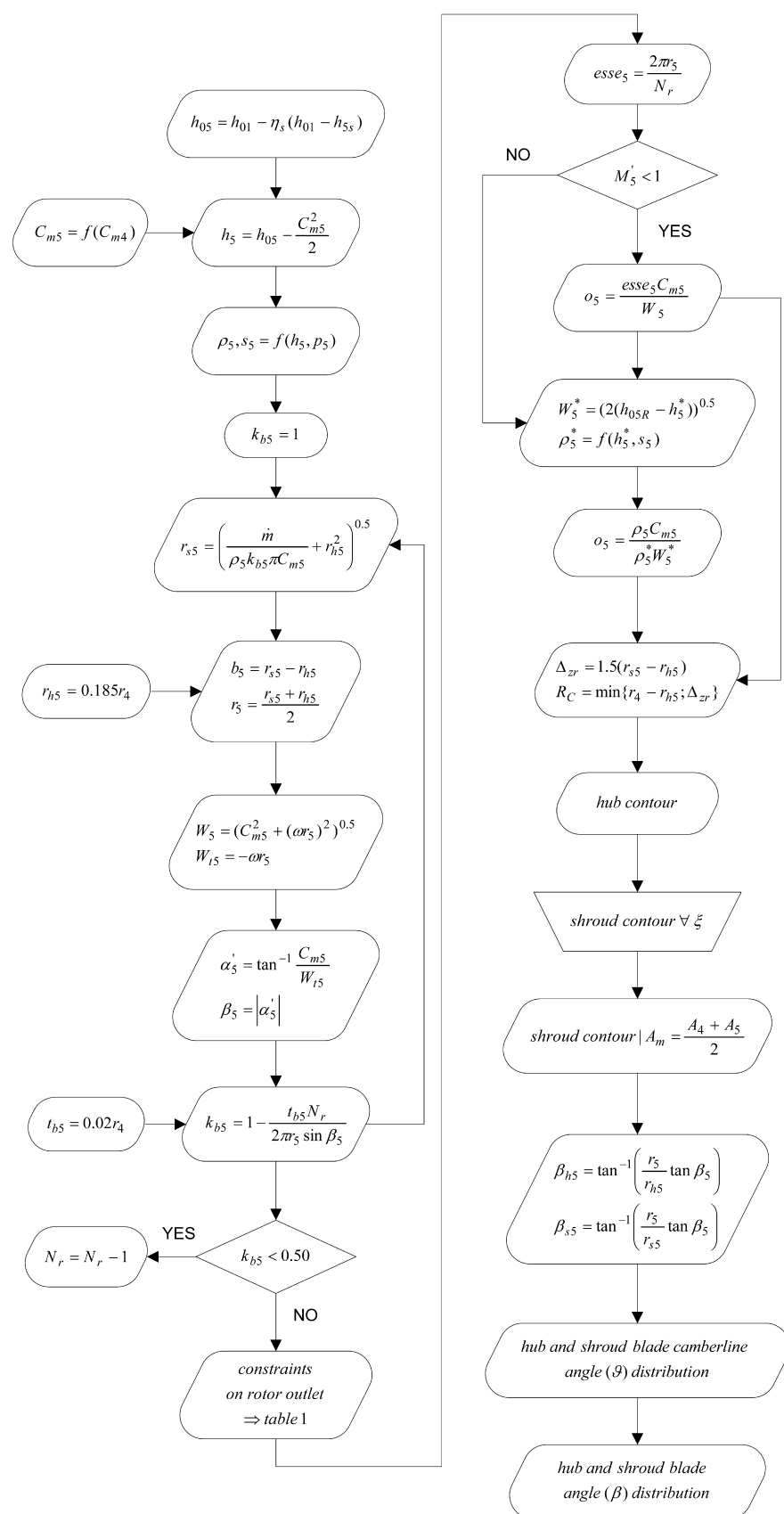


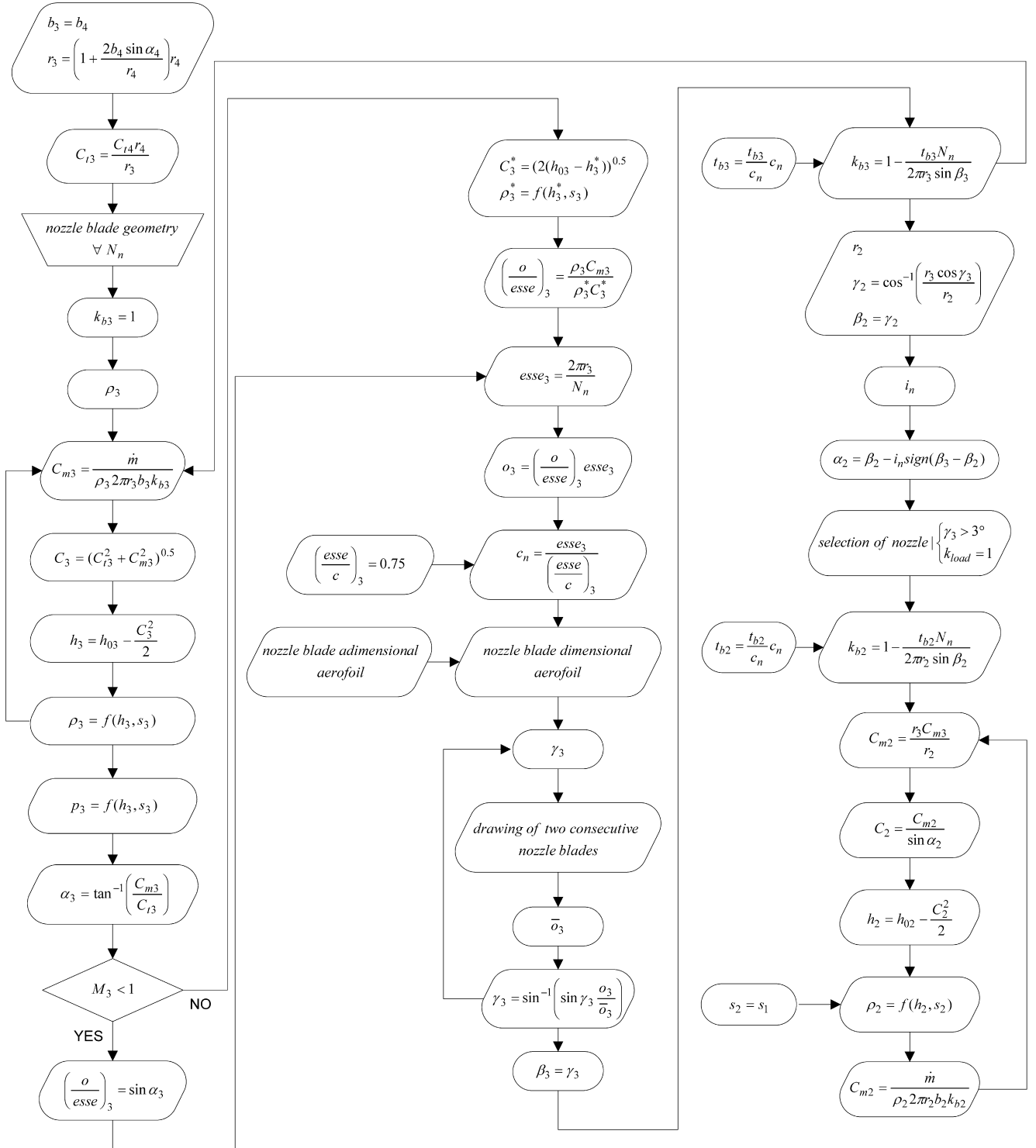
Table 1

Constraints in the sizing of the rotor outlet station.

Maximum shroud radius	$r_{s5} < 0.7r_4$
Minimum hub radius	$r_{h5} > 0.4r_{s5}$
Maximum increase of the flow passage area	$A_5/A_4 < 2.5$

Nozzle throat

Supersonic flow regimes often occur at nozzle outlet due to the high tangential absolute velocity and the low speed of sound typical of high molecular weight fluids. When the Mach number at nozzle outlet (M_3) is higher than one, the nozzle is choked and sonic flow conditions (star superscript) take place at the throat (o_3). The nozzle throat width o_3 is calculated from the pitch ($esse_3$) and the throat-to-pitch ratio ($o/esse$)₃, where the latter derives from the mass flow conservation between

**Fig. 5.** Design of the nozzle.

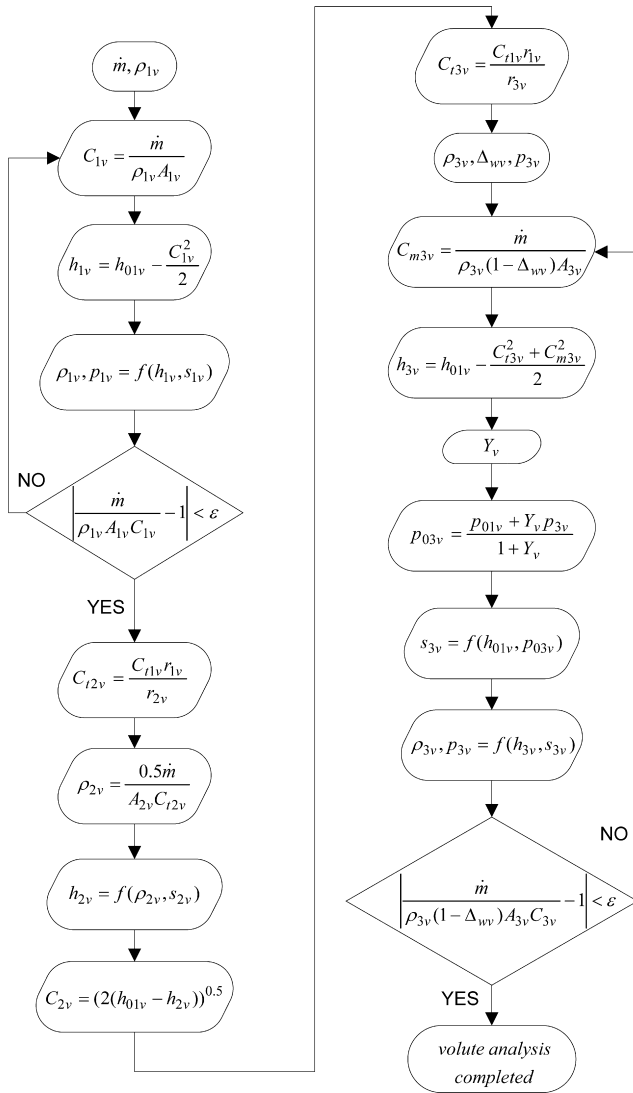


Fig. 6. Performance analysis of the volute.

throat and exit section. The chord of the nozzle blades follows from the assumption on the pitch-to-chord ratio (0.75).

Calculation of the setting angle

Nozzle blades are designed by imposing a thickness distribution on a straight line camberline. Only a specific value of the setting angle (γ_3) yields the throat width o_3 calculated above. Thus, an iterative method is needed to graphically obtain the desired value of the throat width. After a first guess value of γ_3 is chosen, two consecutive blades are drawn and the measured \bar{o}_3 is used to obtain a new estimate of γ_3 until convergence (i.e., $\bar{o}_3 = o_3$).

Nozzle inlet

The setting angle is used to calculate the radius (r_2) and blade angle (β_2) at nozzle inlet. The inlet flow angle (α_2) slightly differs from the blade angle by the optimum incidence angle (i_n) (see [24]). Finally, the nozzle fulfilling a constraint on minimum γ_3 ($> 3^\circ$) and satisfying the optimum blade loading condition is selected. The velocity triangle and thermodynamic state are determined through an iterative mass balance.

2.2. Performance routine

In this Section the general features of the performance routine are first described. Then the procedure used to solve the flow field in each expander component is summarized and shown in detailed flowcharts. Finally, some strategies which were applied to solve specific calculation issues are presented.

Input data

The performance routine is the code section which solves the flow field along the mean line in each expander component (volute, nozzle, annulus, rotor) and finally calculates the expander efficiency (η_i). It uses as input data: (i) the geometry defined by the design routine, (ii) the total inlet state at turbine inlet (p_{01} , T_{01}) and (iii) the specified static pressure at rotor outlet (p_{dis}) (see Fig. 1). Although this routine may potentially be used to calculate the flow field at any operating condition, it is used in this work to predict the flow field and the turbine efficiency at design conditions. Accordingly, the input variables p_{01} , T_{01} do not differ from those specified in the design routine and p_{dis} is the design discharge pressure ($p_{dis} = p_5$).

Loss correlations

Unlike the design routine, which calculates only the inlet and outlet stations of each component, the performance routine solves the flow field at three stations: inlet (subscript 1), mid (2) and outlet (3) for a better analysis of the flow field and, in turn, a more accurate prediction of the losses. The irreversibilities along the expansion process are quantified by the recent loss correlations provided by Aungier [24] in terms of total pressure loss coefficients (Y) included in Appendix A. These irreversibilities are taken into account when solving stations 3 only, since the loss model assumes no entropy increase between stations 1 and 2. However, their estimate depends on the geometrical and kinematic parameters of all three stations.

Iterative mass balances

Iterative mass balances are widely used in the code to solve the flow field. They follow this recurrent scheme: a guess value of static density is first assumed to calculate the velocity from the continuity equation. This allows the evaluation of the static enthalpy from the known total state (static frame) or rothalpy (relative frame) and, in turn, the static pressure and density by means of the equation of state. The new calculated density value updates the guess value and is backward used in the mass balance inside a loop, until convergence on the desired mass flow rate is reached.

Calculation of the mass flow rate entering the turbine

In the performance routine the mass flow rate (\dot{m}) is not given (as it was instead in the design routine), but rather calculated. In fact, for assigned turbine geometry and total conditions at stage inlet, there is only one specific value of mass flow rate resulting in the specified rotor outlet static pressure (p_{dis}). This value slightly differs, yet it is generally close to that assumed in the design routine, due to various effects which were disregarded in the definition of the overall turbine geometry.

2.2.1. Volute

Fig. 6 shows the various steps in the evaluation of the volute performance. The total state at volute inlet (i.e., the stage inlet) is known. The passage area (A_{1v}) and mean radius (r_{1v}) at station 1 are known from the design routine. The tangential velocity at station 2 (C_{t2v}) is calculated from the conservation of angular momentum. Station 3 is the annular passage at volute exit (i.e., nozzle inlet). At this station both the radius and passage width are known from the design routine so that the

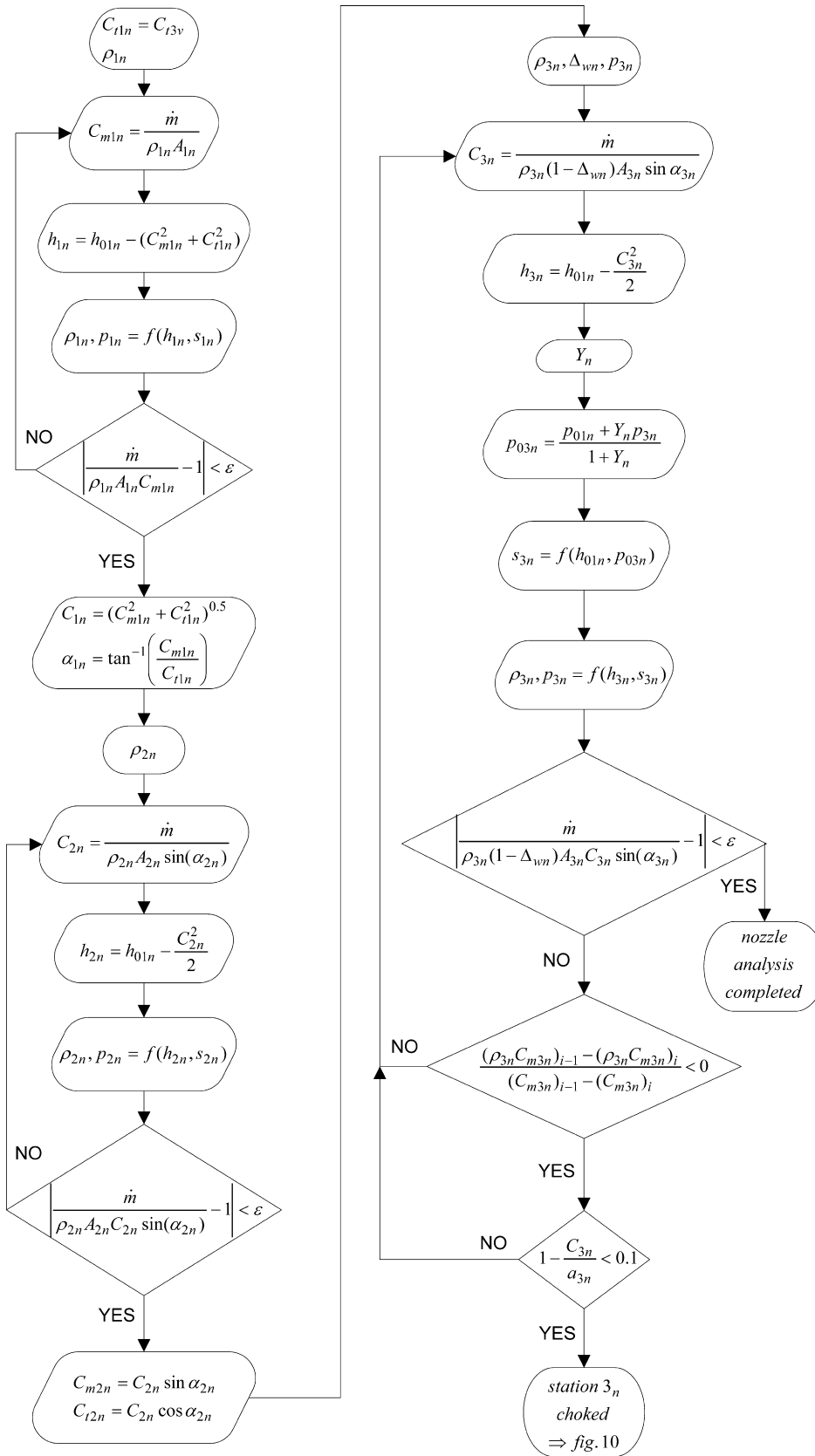


Fig. 7. Performance analysis of the nozzle.

passage area (A_{3v}) can be easily calculated. The solution of the flow field in the volute proceeds with the calculation of the overall loss coefficient (Y_V) (see Appendix A.1). By using the definition of total pressure loss, the total pressure at volute outlet (p_{03v}) is calculated. So,

the entropy and all static variables at volute exit can be obtained. The volute analysis is completed when the convergence on the mass flow rate is reached.

2.2.2. Nozzle

Fig. 7 shows the flowchart to evaluate the performance of the nozzle. The nozzle geometry is specified at the inlet, mid-passage and outlet from the design routine. The tangential velocity at nozzle inlet (C_{t1n}) is equal to the tangential velocity at volute outlet (C_{t3v}). A first guess nozzle inlet density (ρ_{1n}) is assumed to calculate the meridional

velocity (C_{m1n}) and, in turn, the static enthalpy (h_{1n}). A new value of density is calculated from the couple (h_{1n} , $s_{1n} = s_{3v}$) which updates the previous one till convergence. So, the velocity triangle at nozzle inlet is defined and the flow angle (α_{1n}) can be calculated. A guess value is assumed for density at station 2 (ρ_{2n}) to calculate C_{m2n} . The velocity C_{2n} is calculated by assuming that the flow angle is equal to the blade angle

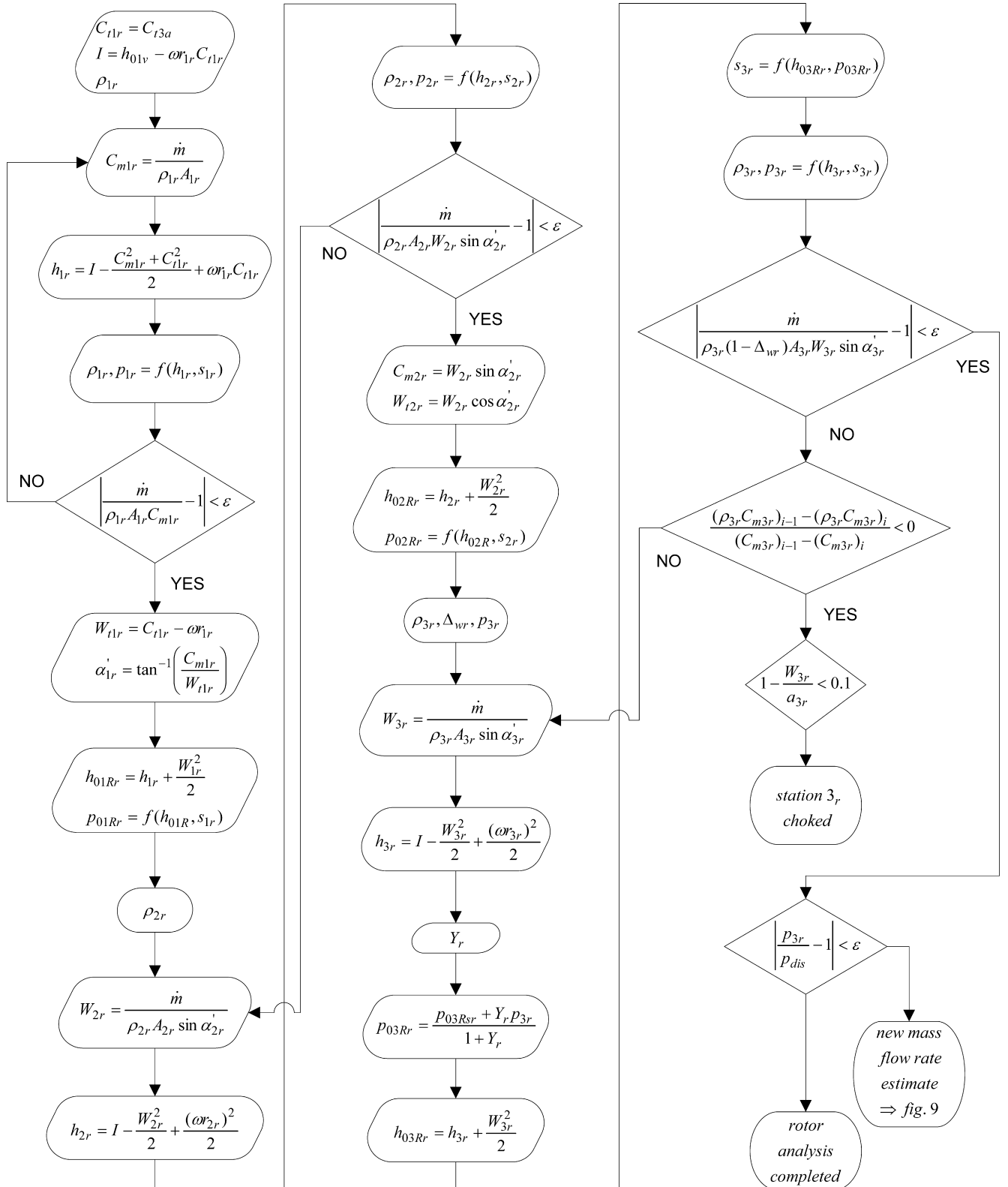


Fig. 8. Performance analysis of the rotor.

($\alpha_{2n} = \beta_{2n}$). Accordingly, the static enthalpy (h_{2n}) and all the static properties at station 2 can be obtained (being $s_{2n} = s_{1n}$). After reaching convergence, station 2 is solved. Then, guess values are assumed for the density (ρ_{3n}) and pressure (p_{3n}) at nozzle outlet which allows the velocity (C_{3n}) and static density (h_{3n}) to be calculated.

The solution of the flow field in the nozzle proceeds with the calculation of the overall loss coefficient (Y_n) (see Appendix A.2). The incidence loss is null by ensuring that the flow angle at nozzle inlet deviates from the blade angle by the optimum incidence angle ($\alpha_{1n} = \beta_{1n} - i^*$). The profile loss is calculated by using the main geometrical features of the nozzle, the fluid velocities and the number of blades. The post-expansion loss accounts for shock losses occurring at supersonic flow conditions often experienced by organic fluids.

From the definition of total pressure loss coefficient the total pressure at nozzle outlet (p_{03n}) can be directly calculated. Consequently, the entropy and all the remaining static properties at nozzle outlet are obtained. At subsonic flow conditions the nozzle design is terminated when the convergence on ρ_{3n} and p_{3n} is reached. Instead, if the nozzle is choked (i.e., the two inequalities in the lower right part of the flowchart in Fig. 7 are verified) further steps are needed to achieve the solution, which are described in Section 2.2.5 (i.e., the flowchart continues in Fig. 10).

2.2.3. Rotor

Fig. 8 shows all the steps required to evaluate the performance of the rotor. The rotor passage geometry is defined at the inlet, mid-passage and outlet stations from the design routine (see [24]). The tangential component of absolute velocity at rotor inlet (C_{1r}) is equal to that at annulus outlet (C_{13a}). Rothalpy (I) is conserved through the rotor and can be directly calculated from the total enthalpy at stage inlet and C_{1r} . The density assumption at rotor inlet (ρ_{1r}) allows the meridional velocity (C_{m1r}) to be calculated. So, the static enthalpy at rotor inlet (h_{1r}) can be obtained and, in turn, all the remaining static thermodynamic variables (being $s_{1r} = s_{3a}$). After achieving convergence on ρ_{1r} the velocity triangle at rotor inlet is fully determined. Moreover, the relative total enthalpy (h_{01Rr}) and relative total pressure (p_{01Rr}) can be calculated. By assuming a guess value for ρ_{2r} the relative velocity and static enthalpy (h_{2r}) can be calculated. Accordingly, all the static properties at station 2 are obtained, the velocity triangle is fully defined and the total relative enthalpy and pressure can be calculated. Finally, guess values are assumed for ρ_{3r} and p_{3r} . These allow the calculation of the relative velocity (W_{3r}) and static enthalpy at rotor outlet (h_{3r}).

The solution of the flow field in the rotor proceeds with the calculation of the overall loss coefficient (Y_r) using the main geometrical features of the rotor and flow velocities. The overall loss coefficient can be ideally subdivided into five loss components, namely profile, incidence, blade loading, hub-to-shroud loading and clearance (see Appendix A.4). The incidence loss can be considered approximately null in this study which considers only design conditions. By the definition of total pressure loss coefficient (note that this is peculiar for the rotor) the relative total pressure at rotor outlet can be calculated (p_{03Rr}). In addition, the relative total enthalpy at rotor outlet (h_{03Rr}) can be calculated from the rothalpy and exit radius. So, the entropy at rotor outlet (s_{3r}) can be calculated which, combined with h_{3r} , gives all the remaining static properties. After the convergence on ρ_{3r} and p_{3r} is achieved a final check is done to ensure that p_{3r} is equal to the specified discharge pressure (p_{dis}). If this is not verified, the overall performance analysis is repeated for a new estimate of the mass flow rate until the final value is obtained. Instead, if the convergence on ρ_{3r} and p_{3r} cannot be achieved and the inequality describing the onset of choking is verified, the rotor is choked and further calculations are needed as described in Section 2.2.5.

2.2.4. Calculation of the mass flow rate matching the specified turbine outlet pressure

After all the expander components have been successfully analyzed

in absence of choking, the static pressure at rotor outlet (p_{3r}) is calculated. Fig. 9 shows graphically the iterative scheme used to adjust the mass flow rate up to the final convergence on the specified rotor discharge pressure (p_{dis}). The new estimate of mass flow rate is obtained by applying a linearization of the turbine characteristic between the current ($p_{3r} - \dot{m}$)_i and previous ($p_{3r} - \dot{m}$)_{i-1} couple, where the blue arch is the unknown expander characteristic and the numbers indicate subsequent steps of the iterative procedure. At the beginning of the performance routine a first guess mass flow rate (\dot{m}^I) is chosen and results in the rotor outlet pressure (p_{3r}^I) (i.e., first operation point); the intersection between the straight line r^{0-I} passing through the origin and the point (p_{3r}^I, \dot{m}^I) and the vertical straight line through p_{dis} allows the second estimate of mass flow rate (\dot{m}^{II}) to be obtained; accordingly, the corresponding p_{3r}^{II} is calculated (i.e., second operation point); the intersection between straight line r^{I-II} passing through the last two points of the expander characteristic (still unknown) and the vertical straight line through p_{dis} gives the third estimate of the mass flow rate (\dot{m}^{III}); the corresponding p_{3r}^{III} is calculated (i.e., third operation point), and so on. The iterative scheme converges on the mass flow rate \dot{m}_{pdis} which gives the desired p_{dis} (red dot).

2.2.5. Solution of the flow field when choking occurs

This Section outlines how the performance routine manages the turbine choking. When the iterative mass balance at nozzle or rotor outlet cannot converge, some additional calculations are to be performed as implied by the exits labels “station 3n choked” and “station 3r choked” in Figs. 7 and 8. The aim of this Section is threefold: (i) to present the criterion for the choking detection; (ii) to illustrate the interactive scheme to calculate the maximum swallowing capacity of the expander \dot{m}_{choked} ; (iii) to show how p_{dis} is reached through post-expansion shock waves.

By considering two consecutive iterations (indexes $i-1$ and i) of the above-mentioned mass balances, it may happen that the product of density and meridional velocity ($\rho_3 \cdot C_{m3}$) decreases in spite of the gain in meridional velocity:

$$\frac{(\rho_3 \cdot C_{m3})_i - (\rho_3 \cdot C_{m3})_{i-1}}{(C_{m3})_i - (C_{m3})_{i-1}} < 0 \quad (1)$$

When the inequality in Eq. (1) is verified and the flow velocity is

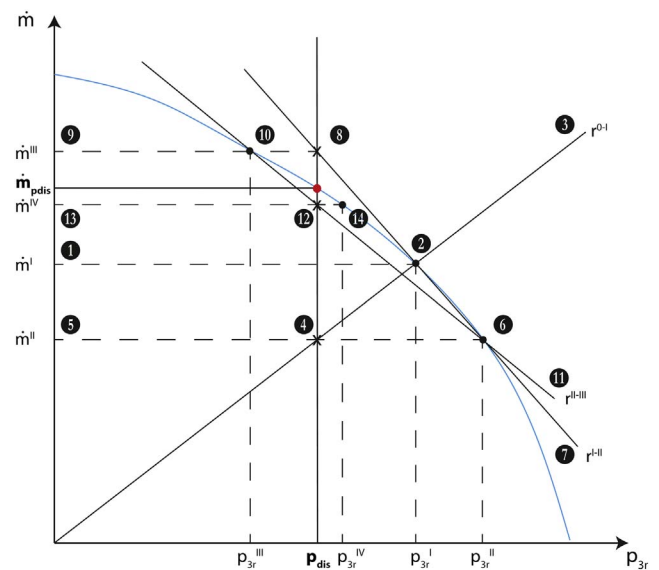


Fig. 9. Graphical interpretation of the iterative scheme to calculate the mass flow rate leading to the specified turbine outlet pressure (p_{dis}). The blue line is the unknown turbine characteristic and the red dot is the convergence operation point. (For interpretation of the references to colours in this figure legend, the reader is referred to the web version of this paper.)

higher than 90% of the local speed of sound (to avoid false choking detections), the examined station is certainly choked.

When choking occurs, the model iteratively seeks for the choking mass flow rate (\dot{m}_{choke}), which represents the maximum swallowing capacity of the expander. In more detail, let us call \dot{m}_{max} and \dot{m}_{min} two mass flow rates higher and lower than the searched choking mass flow rate. If using the current mass flow rate estimation (\dot{m}) the mass flow rate balance on the originally choked station 3 converges, then the subsequent mass flow rate estimate is increased towards \dot{m}_{max} . Instead, if the mass flow rate balance ends again with a choking detection, then the subsequent mass flow rate estimate is reduced towards \dot{m}_{min} . In this way, the difference between \dot{m}_{max} and \dot{m}_{min} is progressively reduced until convergence on \dot{m}_{choke} . When \dot{m}_{choke} is found, the post-expansion calculations outlined in the following paragraphs can be performed. Choking usually occurs at nozzle outlet (station 3n) and, more rarely, at rotor outlet (station 3r) or at the outlet of both rows. Thus, only the calculation procedure used for nozzle outlet choking is shown for brevity.

Nozzle choking

When choking occurs at nozzle outlet a proper static pressure at nozzle outlet (p_{3n}) after post-expansion is searched, such that the calculated rotor outlet pressure p_{3r} matches the specified discharge pressure (p_{dis}). The convergence procedure is iterative and requires all calculations downstream the choked station 3n to be repeated for each new estimation of p_{3n} (i.e., the annulus and rotor analyses).

Fig. 10 shows all the steps involved in the procedure where p_{max3n} and p_{min3n} are the pressures after the nozzle post-expansion resulting in p_{3r} values respectively higher and lower than p_{dis} (i.e., the target p_{3n} value falls between p_{max3n} and p_{min3n}). The static properties at nozzle outlet (h_{3n} , ρ_{3n}) are calculated from guesses for the entropy at the onset of choking (s_{3n}) and pressure (p_{3n}). Accordingly, the absolute velocity (C_{3n}) and flow angle (α_{3n}) at nozzle outlet can be calculated. Then, the total pressure loss coefficient (Y_{exr}) is calculated and, in turn, the total pressure at nozzle outlet (p_{03n}). So, a new value of s_{3n} is calculated until convergence. Note that in the flowchart p_{03n}^{ch} is the nozzle outlet total pressure at the onset of choking. The analysis proceeds with the calculation of the flow field in the annulus and rotor. If the resulting rotor outlet pressure (p_{3r}) is different from the specified discharge pressure then the first guess value of nozzle outlet pressure (p_{3n}) is adjusted until convergence.

3. Results

3.1. Limitations of the common correlations of turbine efficiency with specific speed and velocity ratio

Turbine efficiency is commonly correlated with the specific speed (n_s). The total-to-static efficiency (η_s) at first increases with n_s , reaches a maximum and finally decreases. The well-known losses breakdown obtained by Rohlik [31] for a 90° radial inflow turbine stage shows the main reasons for this trend. At low n_s the main loss contributions (nozzle, rotor, clearance and windage) are significant and gradually diminish at higher n_s . On the other hand, the exit kinetic energy becomes very high at high n_s , thereby reducing η_s . The plot η_s versus n_s in [31] shows that the minimum overall loss occurs in a quite narrow range of n_s between 0.55 and 0.60.

However, the turbine efficiency depends on the velocity ratio (v_s) as well. Aungier in [24] clearly showed that the optimum velocity ratio (v_s) increases as n_s increases. By properly selecting v_s the maximum turbine efficiency is kept quite flat in a wider range of n_s between 0.45 and 0.65. The corresponding optimum v_s varies in a narrow interval centered on 0.65.

While these results are referred to common fluids (air, flue gases) it would be interesting to know whether these design guidelines still

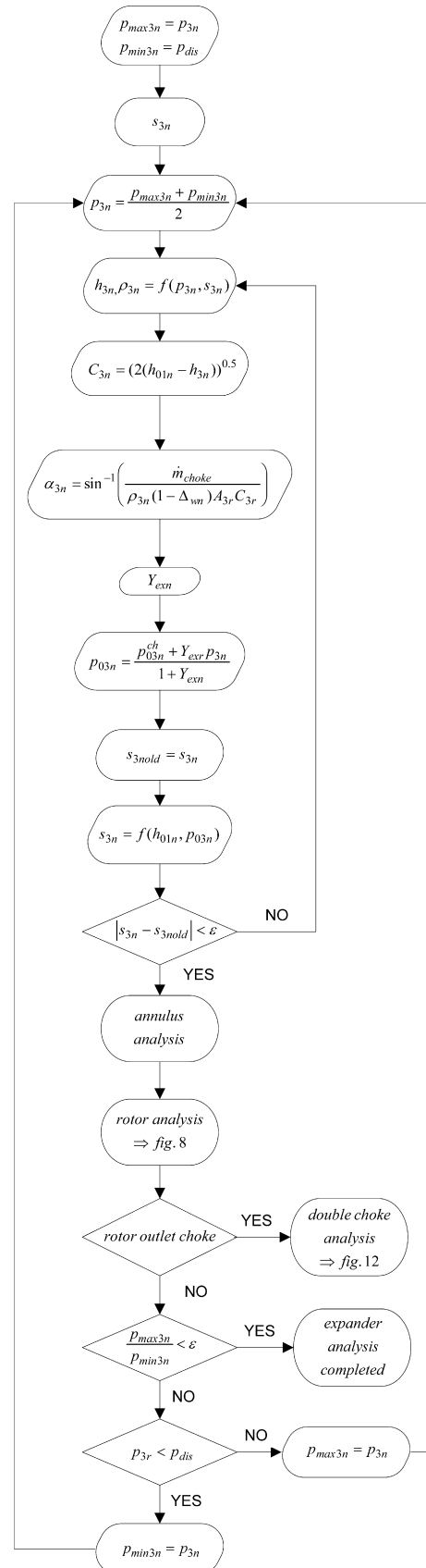


Fig. 10. Solution of the flow field when choking occurs at nozzle outlet.

apply to the high molecular weight fluids typically used in ORC systems. Moreover, it would be interesting to separate the effects on turbine efficiency deriving from non-optimum n_s from those arising from non-optimum v_s . To the authors' knowledge no such 3D maps are available in the literature showing the relationship $\eta_s = f(n_s, v_s)$ for RIT working with organic fluids. Instead, maps are available for RIT working with common fluids which correlate turbine efficiency with two different design parameters, namely the flow coefficient and loading coefficient (see Moustapha et al. [15]) or the specific speed and the specific diameter (see Balje [32]).

Thus, this Section shows the new performance maps generated by the mean-line model described in the previous Sections. These maps update and generalize maps already available in the literature and are used to derive general guidelines for the design of ORC turbines. The new maps are obtained by running the simulation model at multiple (n_s, v_s) couples for various design specifications and considering R245fa as working fluid.

3.2. New maps of turbine efficiency versus specific speed and velocity ratio

3.2.1. Influence of n_s , v_s and VR on turbine efficiency

Fig. 11 shows the turbine efficiency maps $\eta_s = f(n_s, v_s)$ generated by the calculation code developed in this work for two different design specifications. Fig. 11a refers to a working fluid mass flow rate of 20 kg/s and an evaporation temperature of 60 °C (which, considering the properties of R245fa, corresponds to $SP = 0.12$ m and $VR = 2.3$). Fig. 11b refers to a higher evaporation temperature (110 °C) and the same \dot{m} (which gives $SP = 0.10$ m and $VR = 8.7$).

In both maps n_s and v_s are varied within wide intervals (0.30–0.55 and 0.50–0.80, respectively) which include the optimum. The calculated maximum turbine efficiency is 89.4% at low VR (Fig. 11a) and drops to 87.3% at high VR (Fig. 11b). It is noteworthy that the optimum n_s , which is equal to 0.415 regardless of VR, is much lower compared to the optimum range reported in the literature for common gases (see Section 3.1). Instead, the optimum v_s is still centered on 0.65 but is markedly affected by VR: low VR values require higher v_s and vice versa. The lines at constant total-to-static efficiency (η_s) form rotated ellipses not aligned with the axes and tilted above the horizontal. The effect of n_s on turbine efficiency is milder compared to the effect of v_s , as shown by the aspect ratio of the ellipse.

3.2.2. Influence of n_s , v_s and VR on turbine geometry

The turbine designer's choices for n_s directly affect the turbine

geometrical features and, in turn, the efficiency. Fig. 12 shows the shapes of the meridional channels obtained at three different values of n_s and at the optimum v_s for the low VR scenario ($VR = 2.3$). Instead, Fig. 13 refers to the high VR scenario ($VR = 8.7$). It can be easily seen that the rotor inlet radius (r_4) markedly decreases as n_s increases, so that the geometry approaches the axial flow one. At high n_s the specific work is obtained by increasing the rotational speed rather than the rotor radius, and vice versa at low n_s . In addition, at high n_s the blade height required at rotor inlet (b_4) is higher than at low n_s to compensate for the lower circumference. At high VR the blade height at rotor inlet is reduced due to the higher fluid density dictated by the higher pressures compared to the low VR scenario. Moreover, the rotor inlet radius is lower compared to low VR as a consequence of the lower optimum v_s .

3.2.3. Influence of n_s , v_s and VR on loss breakdown

The losses breakdown versus n_s for the low and high VR scenarios is shown in Fig. 14. These plots show a decreasing trend of the nozzle loss as n_s increases which is counter-balanced by the rising trend of the kinetic energy loss. Note that both losses grow in the high VR scenario.

As for the impact of the velocity ratio (v_s) on the loss distribution at optimum n_s a similar trend is obtained, as shown in Fig. 15. As v_s increases the nozzle loss decreases but the rotor loss increases. Moreover, at high VR also the leaving kinetic energy loss markedly increases, also as a consequence of the active constraints in Table 1.

3.3. New maps of turbine efficiency versus size parameter and volumetric expansion ratio

3.3.1. Influence of SP and VR on turbine efficiency

The performance map shown in Fig. 16 is one of the main outcome of this work. It shows the variation of total-to-static efficiency (η_s) versus size parameter (SP) and volumetric expansion ratio (VR), as predicted by the mean-line model where:

$$SP = \frac{\dot{V}_{out}^{0.5}}{\Delta h_s^{0.25}} \quad (2)$$

$$VR = \frac{\dot{V}_{out}}{\dot{V}_{in}} \quad (3)$$

The map collects all the optimum turbine designs generated for different values of the design specifications. More specifically, for each design specification dictated by the thermodynamic cycle analysis, the simulation model searches for the optimum couple (n_s, v_s) that

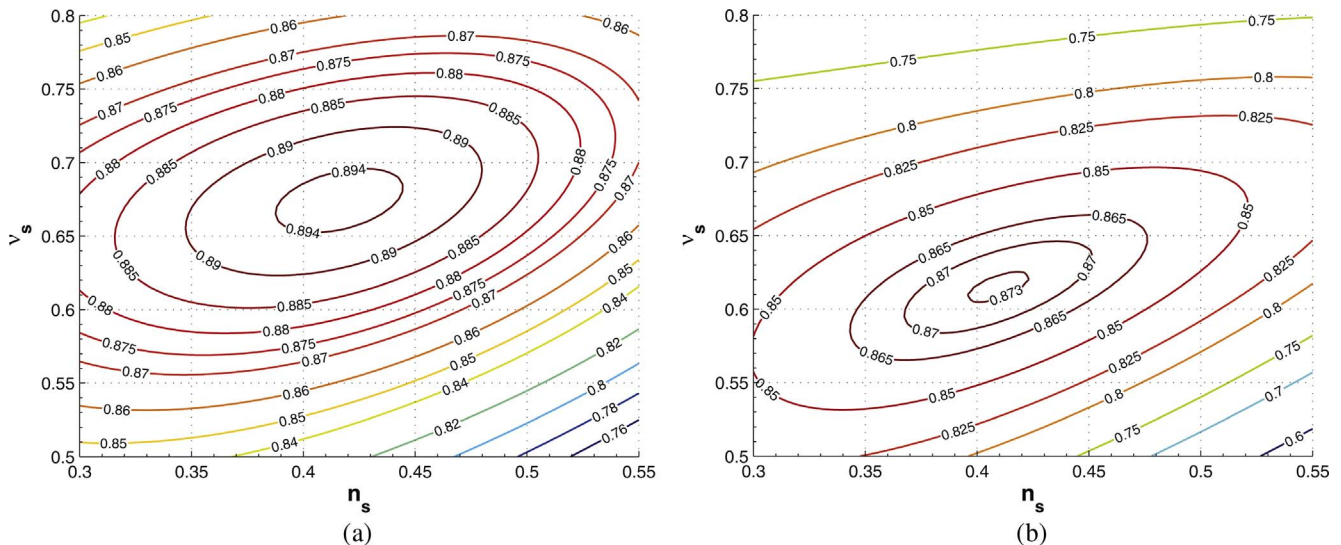


Fig. 11. Total-to-static efficiency (η_s) versus specific speed (n_s) and velocity ratio (v_s): (a) map obtained at low $VR = 2.3$ and $SP = 0.12$ m; (b) map obtained at high $VR = 8.7$ and $SP = 0.10$ m.

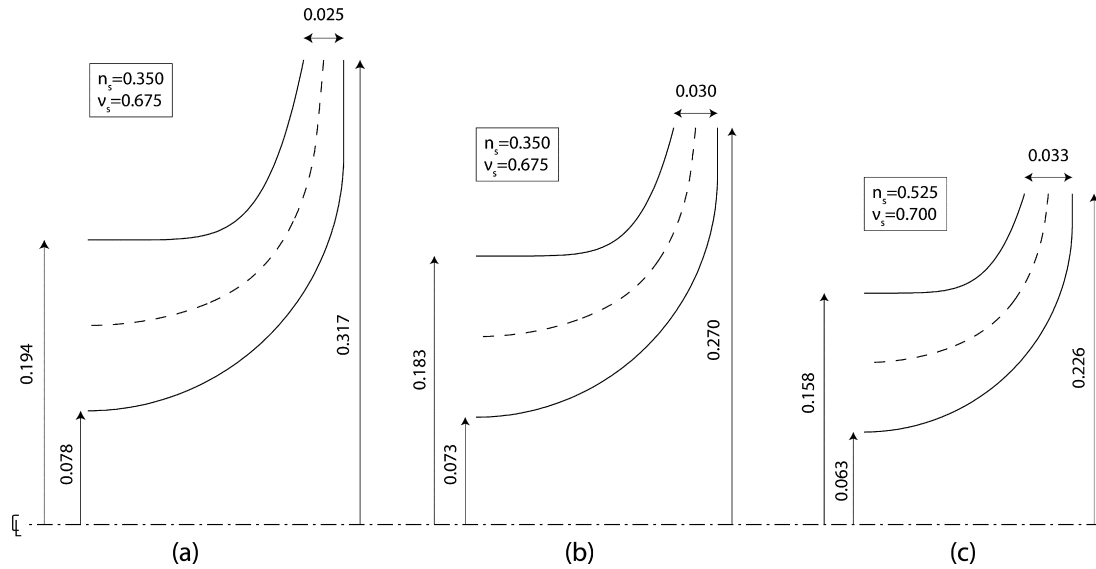


Fig. 12. Shape of the meridional channel for the low VR scenario ($VR = 2.3$ and $SP = 0.12$ m) and different choices of the specific speed: (a) $n_s = 0.350$; (b) $n_s = 0.425$; (c) $n_s = 0.525$.

maximizes η_s . The procedure is repeated for an appropriate set of design specifications which encompass a wide spectrum of mass flow rates (between 0.5 kg/s and 100 kg/s) and evaporation temperatures (between 50 and 130 °C) of the ORC system and a single condensation temperature of 33 °C. By taking into account the thermo-physical properties of R245fa the design specifications can be expressed in terms of SP and VR , shown in the x-axis and y-axis of Fig. 16, respectively.

By intersecting the map with horizontal lines (constant VR) it can be easily noticed that η_s monotonically increases with SP , which shows the positive effect of the turbine size on η_s . The efficiency gain is approximately 3.0–3.5%-points in the considered range of SP . For instance, by intersecting the map at $VR = 4$ the turbine efficiency increases from 86.7% to 90.0%.

A similar monotonic trend of turbine efficiency is not observed for VR . In particular, by intersecting the map with vertical lines (constant SP) it can be noticed that η_s slightly increases up to $VR = 3.6$ –4.0 and then gradually decreases, till the maximum VR considered in this study ($VR = 14$). Thus, there is an optimum VR (slightly lower than 4.0) which maximizes the turbine efficiency and corresponds to the onset of choking conditions. The maximum efficiency drop with VR is in the range 3.0–3.5%-points, regardless of the considered SP . The point in the

map yielding the highest turbine efficiency (90.1%) is located at the maximum SP ($=0.25$) and at $VR = 3.6$. Conversely, the point in the map yielding the lowest efficiency (83.5%) is located in the upper left corner, which is markedly penalized by the combined SP and VR detrimental effects, which count up to 3.3%-points each.

3.3.2. Influence of SP and VR on losses breakdown

To further investigate the trend of turbine efficiency versus SP and VR it is useful to look into the main contributions to the overall loss. Fig. 17a shows the distribution of losses versus SP (at a fixed $VR = 4$). Conversely, Fig. 17b shows the loss breakdown versus VR (at a fixed $SP = 0.075$). By first focusing in Fig. 17a, it can be seen that the losses in the stator (volute and nozzle) and rotor gradually decrease as SP increases, whereas the kinetic energy loss remains quite unaltered. This trend is consistent with that presented in [27]. On the other hand, the increase of VR from 4 up to higher values (Fig. 17b) is accompanied by a marked increase of the losses in the nozzle and the leaving kinetic energy losses. While the increase of the nozzle loss with VR is consistent with [27], the significant increase of the leaving kinetic energy loss is ascribable to the assumption of a maximum passage area ratio of 2.5 between turbine outlet and inlet used in this study (see Table 1).

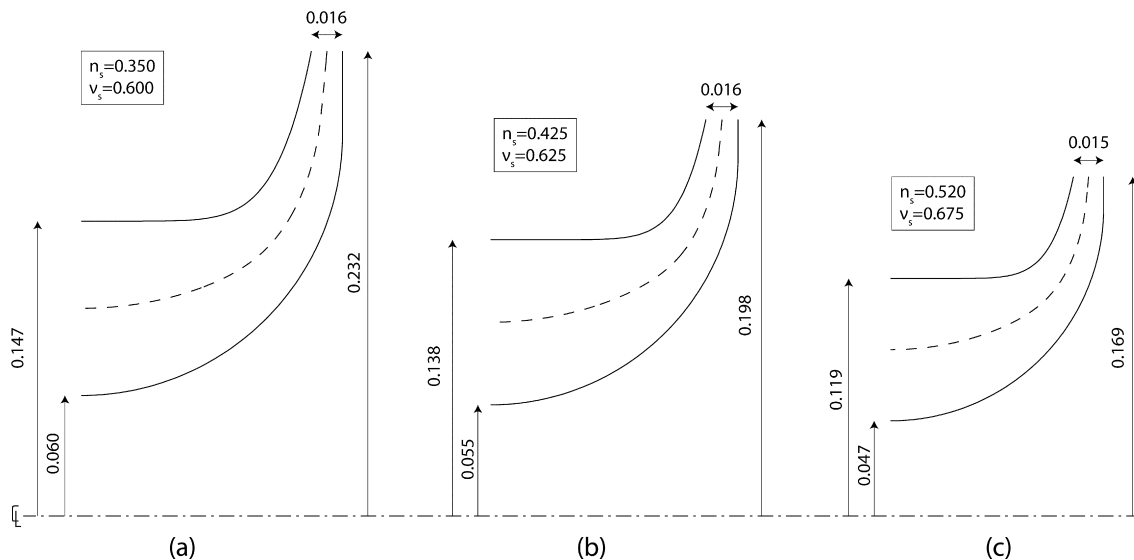


Fig. 13. Shape of the meridional channel for the high VR scenario ($VR = 8.7$ and $SP = 0.10$ m) and different choices of the specific speed: (a) $n_s = 0.350$; (b) $n_s = 0.425$; (c) $n_s = 0.525$.

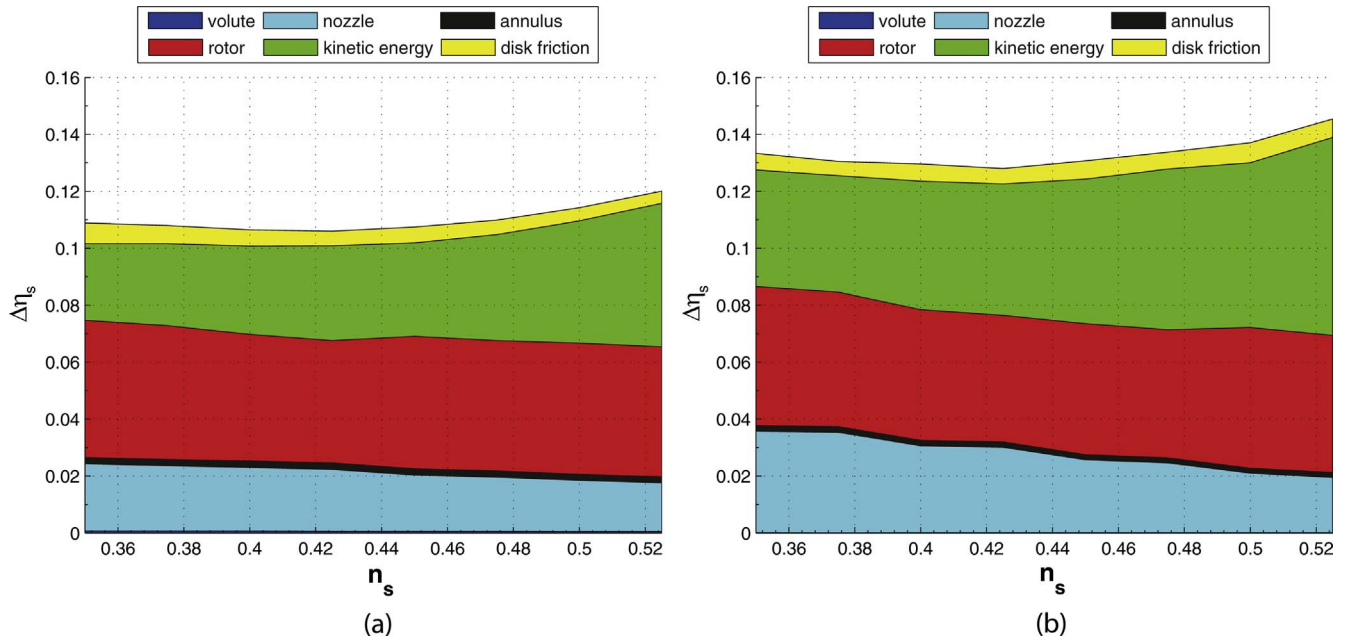


Fig. 14. Distribution of losses versus specific speed for: (a) low VR scenario (VR = 2.3 and SP = 0.12 m); (b) high VR scenario (VR = 8.7 and SP = 0.10 m).

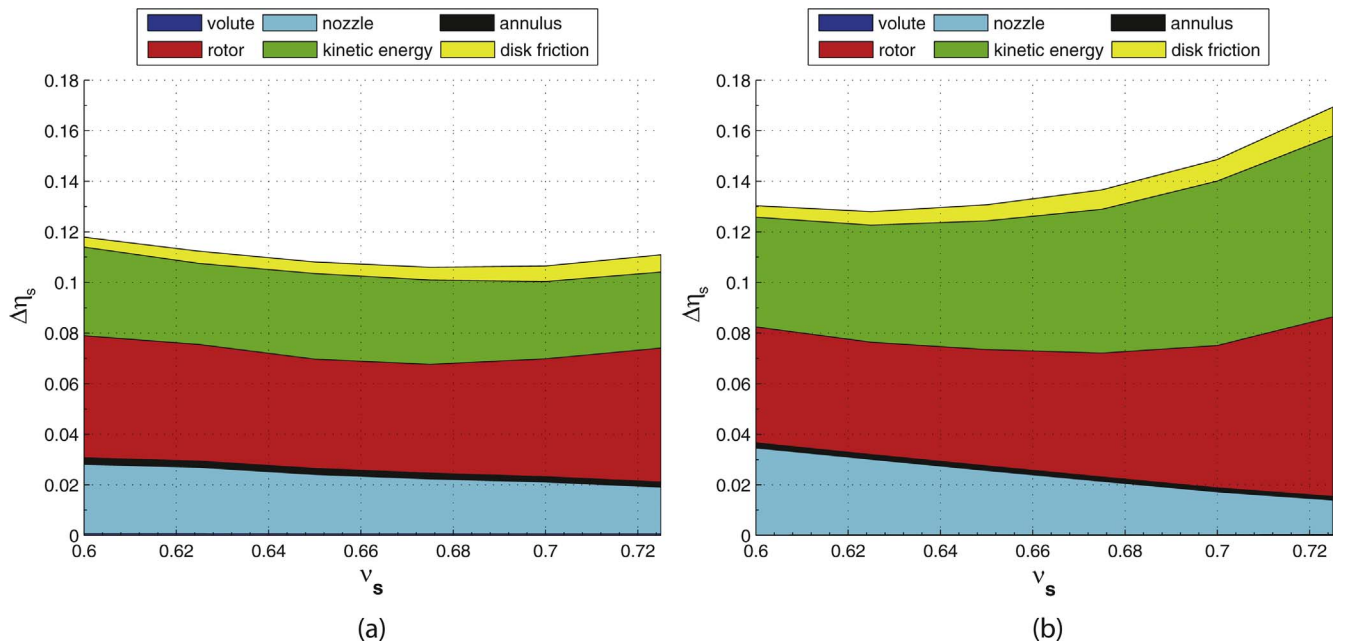


Fig. 15. Distribution of losses versus velocity ratio for: (a) low VR scenario (VR = 2.3 and SP = 0.12 m); (b) high VR scenario (VR = 8.7 and SP = 0.10 m).

4. Critical remarks: validation of the model results

In this Section the reliability of the model results is discussed. Comparisons are made against real plant data in Section 4.1, a relevant (yet dated) study in Section 4.2, recent studies on ORC turbines in Section 4.3 and a recent publication by the authors in Section 4.4.

4.1. Validation against real turbine efficiency data

This work is based on a simulation model expected to give results as close as possible to those measured on the field. At the design conditions, the maximum turbine efficiency reached by the four radial inflow turbines equipping the 48 MW_e (gross) Stillwater geothermal power plant, recently built in Nevada (USA), approaches 90.0% (see [33]). These 12 MW radial expanders were designed by one of the leading

turbine manufacturer in the world and can be considered among the biggest radial expanders operating in ORC systems. Their working point is on the right edge of the map in Fig. 16 and at an average volumetric expansion ratio around 6.0. At these conditions the map predicts a turbine efficiency in the range 89.0–89.5%, which closely agree with the experimental data presented in [33].

4.2. Validation of the mean-line model against Ref. [27]

This work ultimately originates from the study carried out by Perdichizzi and Lozza [27] about thirty years ago where the optimum turbine efficiency was correlated against the size parameter (SP) and the volumetric expansion ratio (VR). Although dated, this is the only map available in the literature showing the dependence of RIT efficiency on SP and VR. This chart is shown for reader convenience in

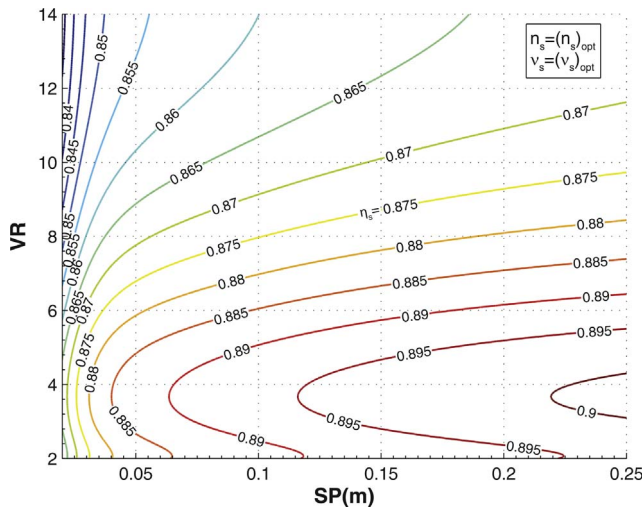


Fig. 16. Total-to-static efficiency (η_s) versus size parameter (SP) and volumetric expansion ratio (VR) at optimum n_s and v_s .

Fig. 18a, and compared with the new map obtained in this work (Fig. 18b) already presented in Fig. 16.

A strong similarity between the two maps leaps out. The main difference is related to the shape of the iso-efficiency lines. Unlike the map obtained in [27] (Fig. 18a) where any increase from $VR = 1$ brought about a reduction of turbine efficiency, in this work (Fig. 18b) the optimum VR is around 3.7–4.0. Moreover, by comparing the total-to-static efficiencies at given values of the size parameter (SP) it can be easily seen that the present work (Fig. 18b) overestimates η_s by 1.0–1.5%-points compared to the original work (Fig. 18a), regardless of VR . The close vicinity of the efficiency values predicted by the two studies can be considered as a sort of validation of the present model. Also comparing the loss breakdown versus VR (Fig. 17b), SP (Fig. 17a) and n_s (Fig. 14) it could be noticed (the reader is referred to the original work [27]) that both the relative magnitude and the trend of the main turbine losses (stator, rotor and leaving kinetic energy) are very similar.

4.3. Validation of the mean-line model against the recent literature on RIT in ORC systems

From the literature survey outlined in the Introduction the following findings can be drawn (see Fig. 19). The specific speeds (n_s) of all RIT designs are within the range 0.40–0.60. Only two turbines were designed using lower specific speeds due to the low power output (only 5 kW_e in [13]) and the limitation on the maximum rotational speed (30,000 rpm in [34]). It is noteworthy that in all studies the optimum velocity ratio (v_s) is lower than 0.7 and varies within the range 0.500–0.690, which is consistent with the findings obtained in this work.

The power outputs of the analyzed turbines vary from 5 kW_e to more than 500 kW_e and the corresponding size parameter between 0.015 and 0.115 m. Accordingly, all turbine designs lie on the left side of Fig. 16. Instead, the volumetric expansion ratio (VR) encompasses a wide range between 2.9 and 53 due to the variety of operating conditions and working fluids. Focusing on R245fa only, VR varies between 3.6 and 29.7, which is well above the maximum VR (i.e., $VR = 14$) analyzed in this work. As summarized in Fig. 19, the total-to-static efficiencies (η_s) of RIT operating with R245fa vary in the range 69.4–84.3% which is quite lower than that shown in Fig. 16. The highest and lowest η_s are achieved by the turbines having the largest size [18] and smallest one [13], respectively.

Also, the methods used to calculate losses have a strong impact on the resulting η_s . Most of the papers use the loss correlations provided by Whitfield and Baines in [11] (see, e.g., Fiaschi et al. [7] and Lang et al.

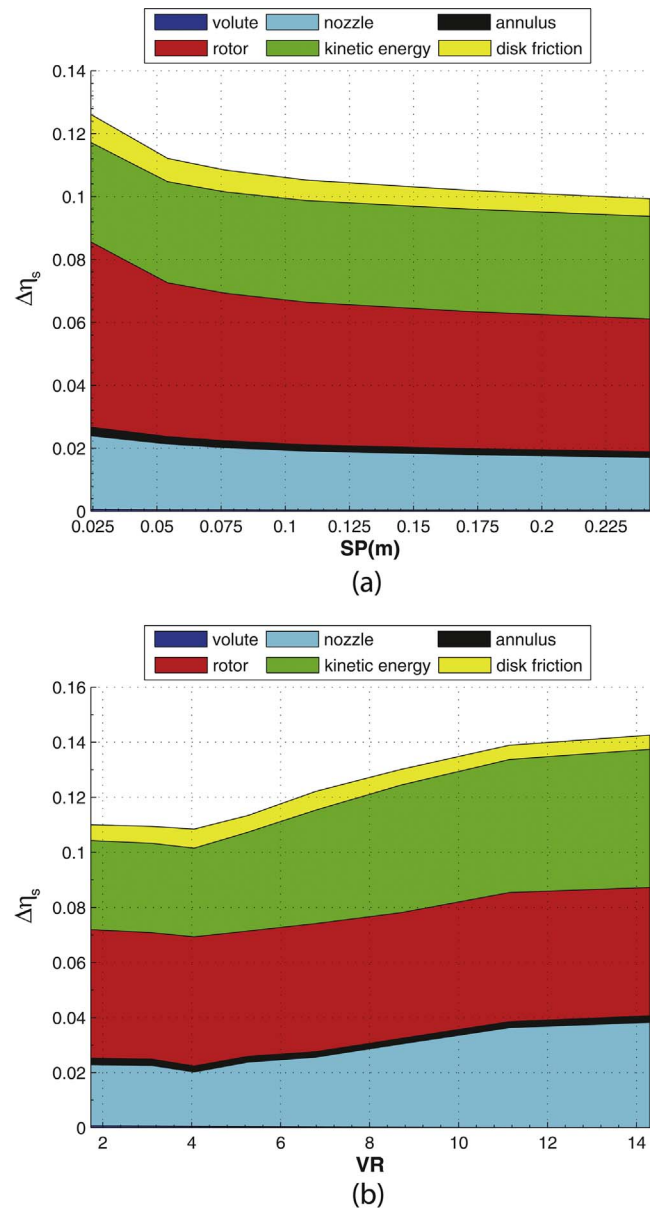


Fig. 17. Distribution of turbine losses as a function of (a) SP (at fixed $VR = 4$); (b) VR (at fixed $SP = 0.075$ m).

[10]). Australian researchers make extensive use of commercial software like RITAL[®] (Sauret et al. [14] and Russel et al. [34]). Chinese researchers (Li et al. [18] and Song et al. [8]) use proper values of the nozzle velocity and rotor velocity coefficients, following the approach described in [35] to calculate nozzle and rotor losses and, in turn, the turbine efficiency. As for UK researchers, Costall et al. [12] follow a similar approach using the nozzle and rotor coefficients suggested by Dixon et al. [36]. Instead Rahbar et al. [9] use loss correlations taken from different sources [11,15] and refined by recent loss models specifically developed for small size radial turbines [37]. None of the studies in the literature uses the recent loss model developed by Aungier [24] to calculate the efficiency of radial turbines for ORC systems. Although the total-to-static efficiencies predicted applying the Aungier's loss correlations are higher compared to the above mentioned studies (as clearly appears by comparing the efficiencies reported in Fig. 19 against those in Fig. 16), the optimum values of n_s and v_s which minimize losses and, in turn, maximize η_s are consistent with the literature. This is an important finding, which confirms the optimum value of specific speed when dealing with organic fluids, which appears

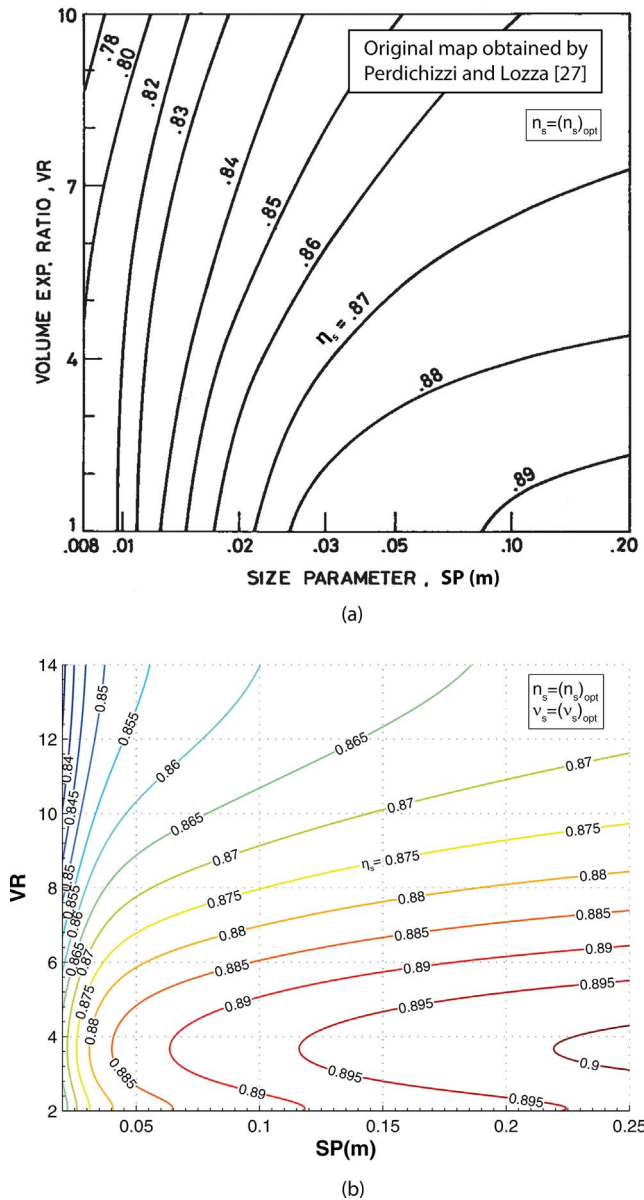


Fig. 18. Comparison between turbine efficiency-SP-VR maps: (a) map obtained by Perdichizzi and Lozza [27]; (b) new map obtained in this work.

lower than that suggested by traditional maps [31].

4.4. Performance comparison between axial flow and radial inflow turbines for ORC systems

By comparing the maps originally obtained by the authors in [38] for ORC axial flow turbines, and further refined in [39] (Fig. 20a), against that obtained in this work for ORC RIT (Fig. 20b) (already presented in Fig. 16 and Fig. 18b), it can be easily noticed that radial turbines can achieve slightly higher efficiencies compared to axial ones in the whole spectrum of SP-VR. While this result is certainly the outcome of some peculiar assumptions (e.g., clearance values used, etc.) which strongly affect performance, yet it can be seen that the optimum VR of axial flow turbines (between 2 and 2.5) is much lower compared to radial ones (around 3.7–4.0). So, the latter turbine design shows a comparatively smaller efficiency decay at high volumetric expansion

ratios. For instance, at VR = 8 the total-to-static efficiency (η_t) predicted for axial turbines varies between 84.5% and 86.2%, whereas in the same SP range then η_t of RIT varies between 86.9 and 88.2%. Thus, RITs appear more suitable to operate under the high expansion ratios and small sizes typical of ORC systems.

5. Conclusions

This work shows how the design choices and working conditions affect the efficiency of radial inflow turbines operating with R245fa. While focusing on a single working fluid, the results obtained are applicable to a wider range of high molecular weight working fluids typically used in ORC systems.

The new efficiency maps generated extend those available in the literature by encompassing sub-optimum design choices, a wider spectrum of working conditions and the behavior of real fluids. In particular, the $\eta_s - n_s - v_s$ picture proposed in this work is new in the literature, which mainly focused on the impact of n_s , while disregarding the additional degree of freedom provided by v_s . Instead, the $\eta_s - SP - VR$ picture updates the valuable early work [27] carried out in the late eighties, by taking advantage of the advances in terms of calculation tools, accurate fluid properties and recent loss correlations matured by the scientific community in the last thirty years.

As for the design choices:

- the optimum specific speed (n_s) lies within a narrow range between 0.41 and 0.42 regardless of the expansion ratio. This value is approximately 25% lower compared to that suggested for common gases (air, flue gases), but consistent with the optimum values suggested by the most recent studies on ORC radial turbines;
- the optimum velocity ratio (v_s) approaches the value of 0.70, traditionally regarded as optimum, only at low expansion ratios. Instead, at the high expansion ratios typical of ORC turbines, it decreases approaching 0.60.

As for the working conditions:

- the optimum volumetric expansion ratio (VR) is around 3.7–4.0, which is higher compared to that of axial flow turbines. At higher expansion ratios the efficiency decline is moderate and is mainly due to the onset of supersonic flow conditions at nozzle outlet and the increase of the leaving kinetic energy loss at rotor exit. The efficiency decay is approximately equal to 3%-points when the volumetric expansion ratio increases from 4.0 to 12.0;
- the turbine size has a remarkable detrimental effect on efficiency when the power range is lower than 50 kW_e, which roughly corresponds to a size parameter (SP) of 0.025 m.

Thus, radial inflow turbines represent a suitable design which provides high total-to-static efficiencies in the range 85–90%, even in presence of high expansion ratios typical of high efficiency ORC systems, when the system size is higher than 50 kW_e. Instead, when the size is lower they undergo a rapid decline of their performance.

While the predicted efficiencies may appear high when compared to the recent literature on ORC systems, yet they are the outcome of a novel and detailed performance analysis procedure, which takes into account the advances in the turbine technology through proper loss correlations. Although only CFD analyses and experimental campaigns can validate these results, the optimum values of the design parameters (n_s and v_s) and the trend of turbine efficiency versus the working conditions (SP and VR) can be considered reliable in spite of the absolute values of turbine efficiency really achieved.

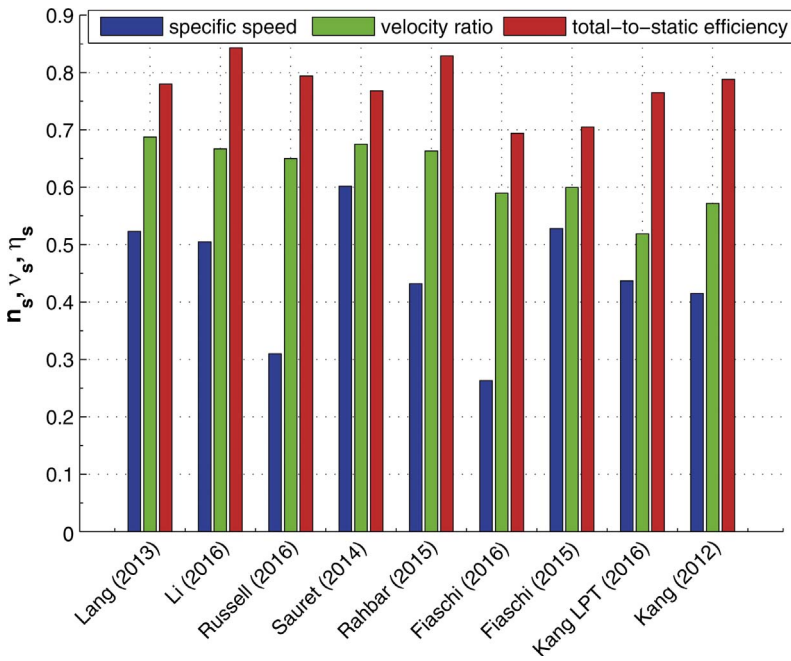


Fig. 19. Values of specific speed, velocity ratio and turbine total-to-static efficiency obtained by recent studies in the literature about ORC RIT. For each study only the first author and the publication year is shown for brevity.

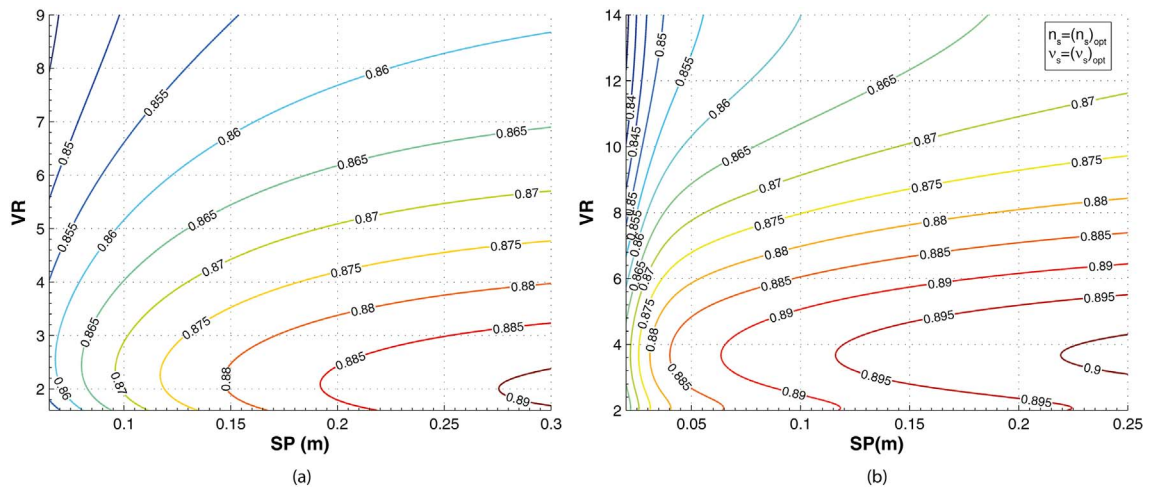


Fig. 20. Comparison between turbine efficiency-SP-VR maps: (a) map obtained by the authors in [39] for axial flow turbines and R245fa; (b) map obtained in this work for RIT and the same fluid. Note the different range of variation of VR.

Appendix A. Loss correlations

A.1. Volute

The total pressure loss coefficient in the volute (Y_v) is defined by:

$$Y_v = \frac{p_{01v} - p_{03v}}{p_{03v} - p_{3v}} \quad (\text{A.1})$$

This coefficient can be expressed as the sum of two components: the profile loss (Y_{pv}) and the circumferential distortion loss ($Y_{\theta v}$):

$$Y_v = Y_{pv} + Y_{\theta v} \quad (\text{A.2})$$

The profile loss coefficient (Y_{pv}) is calculated according to the boundary layer theory:

$$Y_{pv} = \frac{2 \cdot \Theta_v + \Delta_v^2}{(1 - \Delta_v)^2} \quad (\text{A.3})$$

where $\Theta_v = 2 \cdot (\theta_{wv} / b_{3v})$ and $\Delta_v = 2 \cdot (\delta_{wv}^* / b_{3v})$.

The estimation of the boundary layer “momentum thickness” (θ_{wv}) requires the calculation of the skin friction coefficient (c_{fv}), the average density throughout the volute (ρ_{avev}), the flow path length (L_v) and the flow velocities at the three stations (1, 2 and 3):

Table B1
Design data.

Scenario	1	2
<i>Design specifications</i>		
Fluid	R245fa	R245fa
\dot{m} (kg/s)	20	20
T_{01} (°C)	65	115
p_{01} (bar)	4.63	15.70
p_5 (bar)	1.976	1.976
<i>Designer choices</i>		
n_s	0.45	0.45
v_s	0.65	0.65
<i>Rotor</i>		
r_4 (m)	0.246	0.194
N_r	23	23
β_4 (°)	90	90
k_{b4}	0.85	0.85
b_4 (m)	0.032	0.015
r_{s5} (m)	0.170	0.133
r_{h5} (m)	0.068	0.054
b_5 (m)	0.102	0.079
β_5 (°)	31.5	33.7
Δz_r (m)	0.153	0.118
$esse_5$ (m)	0.033	0.026
o_5 (m)	0.0170	0.0142
<i>Nozzle</i>		
b_3 (m)	0.032	0.015
b_2 (m)	0.032	0.015
r_3 (m)	0.260	0.201
o_3 (m)	0.0122	0.0102
c_n (m)	0.0752	0.0701
γ_3 (°)	9.0	6.5
r_2 (m)	0.28	0.22
γ_2 (°)	24.3	24.2
β_2 (°)	24.3	24.2
N_n	29	27
<i>Volute</i>		
r_1 (m)	0.377	0.277
A_1 (m)	0.030	0.011

$$\theta_{wv} = c_{fv} \cdot \rho_{avev} \cdot [(C_{1v}/C_{3v})^5 + 2 \cdot (C_{2v}/C_{3v})^5 + 1] \cdot \frac{L_v}{8 \cdot \rho_{3v}} \quad (\text{A.4})$$

The “displacement thickness” (δ_{wv}^*) can be directly obtained from θ_{wv} by multiplication for the shape factor ($H = 1.2857$).

The circumferential distortion loss ($Y_{\theta v}$) accounts for mixing losses associated with circumferentially non-uniform angular momentum imposed at the volute exit:

$$Y_{\theta v} = \left(\left(\frac{r_{1v} \cdot C_{1v}}{r_{3v}} - C_{t3v} \right) / C_{3v} \right)^2 \quad (\text{A.5})$$

In this study the volute is designed to maintain uniform angular momentum in the circumferential direction so this loss is null ($Y_{\theta v} = 0$).

A.2. Nozzle

The total pressure loss coefficient in the nozzle (Y_n) is defined by:

$$Y_n = \frac{p_{01n} - p_{03n}}{p_{03n} - p_{3n}} \quad (\text{A.6})$$

This coefficient can be expressed as the sum of two loss contributions, namely the profile loss (Y_{pn}) and the incidence loss (Y_{incn}):

$$Y_n = Y_{pn} + Y_{incn} \quad (\text{A.7})$$

The profile loss is calculated from the boundary layer theory as

$$Y_{pn} = \frac{2 \cdot \Theta_n + \Delta_n^2}{(1 - \Delta_n)^2} \quad (\text{A.8})$$

where

$$\Theta_n = 1 - [1 - 2 \cdot (\theta_{wn}/b_{wn})] \cdot [1 - (\theta_{bsn}/b_{bn} + \theta_{bpn}/b_{bn})] \quad (\text{A.9})$$

$$\Delta_n = 1 - [1 - 2 \cdot \delta_{wn}^*/b_{wn}] \cdot [1 - (\delta_{bsn}^*/b_{bn} + \delta_{bpn}^*/b_{bn})] \quad (\text{A.10})$$

Table B2
Performance data.

Scenario	1	2
<i>Volute</i>		
h_{01v} (kJ/kg)	453.5	486.9
p_{01v} (kPa)	462.6	1569.8
$C_{t1v} = C_{1v}$ (m/s)	26.6	22.0
C_{t3v} (m/s)	35.6	27.7
Y_v	0.0150	0.0226
p_{03v} (kPa)	462.3	1568.9
C_{m3v} (m/s)	14.7	11.6
C_{3v} (m/s)	38.5	30.0
α_{3v} (°)	22.5	22.8
p_{3v} (kPa)	444.1	1529.4
<i>Nozzle</i>		
C_{m1n} (m/s)	15.8	12.4
α_{1n} (°)	23.9	24.1
C_{1n} (m/s)	38.9	30.3
p_{1n} (kPa)	443.8	1528.7
Y_{pn}	0.0707	0.1009
Y_{exn}	/	0.0674
Y_n	0.0707	0.1683
p_{03n} (kPa)	452.3	1456.0
C_{m3n} (m/s)	25.3	44.5
C_{t3n} (m/s)	114.9	180.5
α_{3n} (°)	12.4	13.8
C_{3n} (m/s)	117.7	185.9
M_{3n}	0.86	1.36
p_{3n} (kPa)	311.4	582.9
<i>Annulus</i>		
C_{m1a} (m/s)	22.5	35.4
C_{t3a} (m/s)	122.0	187.2
Y_a	0.0067	0.0081
p_{03a} (kPa)	451.3	1448.7
C_{m3a} (m/s)	25.2	39.9
C_{3a} (m/s)	124.6	191.4
p_{3a} (kPa)	297.0	550.2
<i>Rotor</i>		
ω (rad/s)	469	942
I (kJ/kg)	439.4	452.8
h_{03Rr} (kJ/kg)	441.0	456.6
p_{03Rsr} (kPa)	229.9	297.5
Y_{pr}	0.1520	0.1868
Y_{incr}	0.0006	0.0006
Y_{blr}	0.0590	0.0474
Y_{lsr}	0.0518	0.0450
Y_{clr}	0.0881	0.1081
Y_r	0.3515	0.3878
p_{03Rr} (kPa)	221.5	269.6
p_{3r} (kPa)	197.6	197.6

Table B3
Turbine losses and efficiency.

Scenario	1	2
Y_v	0.0150	0.0226
Y_n	0.0707	0.1683
Y_a	0.0067	0.0081
Y_r	0.3515	0.3878
Y_{tot}	0.4439	0.5868
SP (m)	0.12	0.10
VR	2.3	8.7
η_s (%)	88.9	86.9

In Eq. (A.9) three “momentum thicknesses” appear which are related to the wall of the nozzle (θ_{wn}), the blade suction side of the nozzle (θ_{bsn}) and the blade pressure side (θ_{psn}). The dimensional lengths used at the denominator are:

$$b_{bn} = esse_{3n} \cdot \sin \beta_{3n} \quad (\text{A.11})$$

$$b_{wn} = b_{3n} \quad (\text{A.12})$$

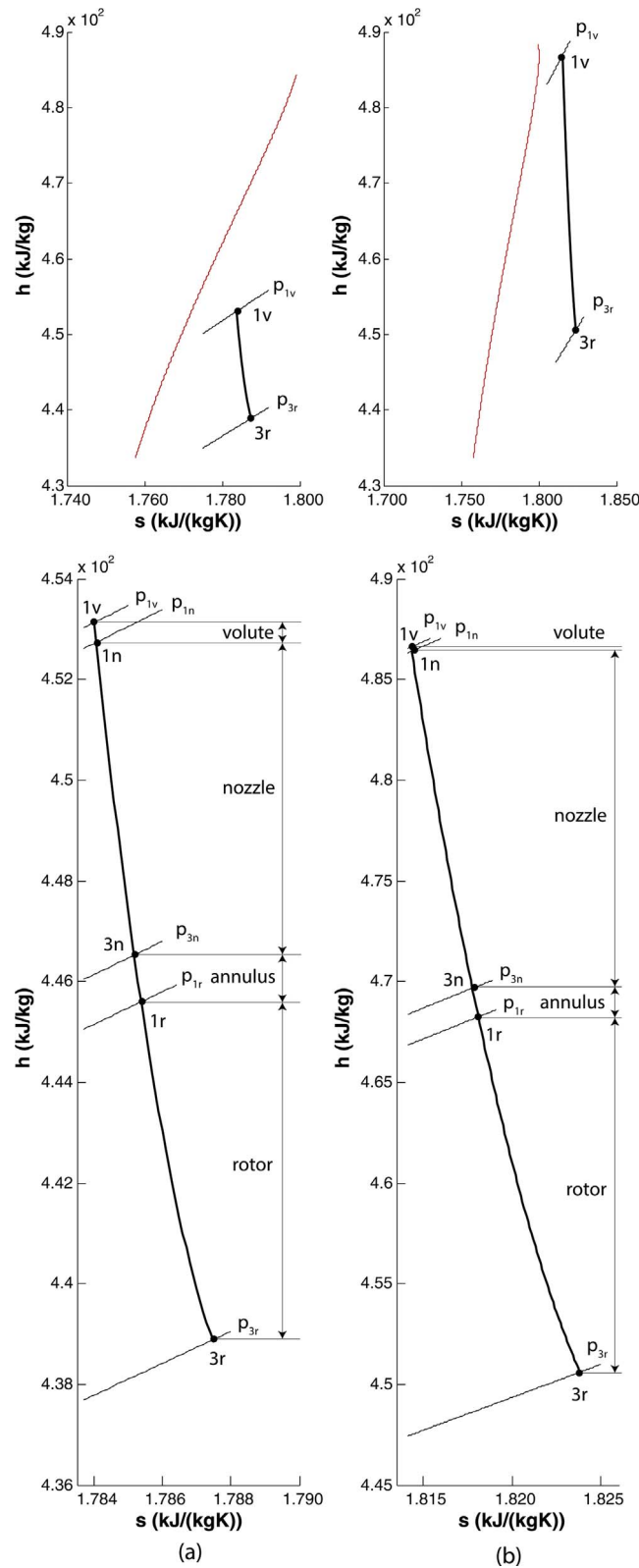


Fig. B1. Expansion lines in the h - s diagram: (a) scenario 1 (i.e., low VR); (b) scenario 2 (i.e., high VR). The red line is the saturation vapor curve.

The incidence loss is:

$$Y_{incn} = \sin^2(\alpha_{1n} - \alpha_{1n}^*) \cdot [p_{01n} - p_{1n}] / [p_{03n} - p_{3n}] \quad (\text{A.13})$$

where α_{1n}^* is the optimum rotor inlet flow angle. This loss is approximately null in this study because only design conditions are considered.

When the flow regime at nozzle outlet is supersonic post-expansion shock waves occur. The associated losses are estimated using the following correlation taken from axial flow cascades:

$$Y_{exn} = \left(\frac{M_{3n}-1}{M_{3n}} \right)^2 \quad (\text{A.14})$$

which is added to the nozzle total pressure loss calculated at sonic conditions.

$$Y_{n|M_{3n} > 1} = Y_{n|M_{3n}=1} + Y_{exn} \quad (\text{A.15})$$

A.3. Vaneless annular passage

The total pressure loss coefficient in the annulus (Y_a) is defined by:

$$Y_a = \frac{p_{01a} - p_{03a}}{p_{03a} - p_{3a}} \quad (\text{A.16})$$

This is the sum of two components, the profile loss (Y_{pa}) and the entrance loss (Y_{ina}):

$$Y_a = Y_{pa} + Y_{ina} \quad (\text{A.17})$$

The profile loss is calculated from the boundary layer theory as:

$$Y_{pa} = \frac{2 \cdot \Theta_a + \Delta_a^2}{(1 - \Delta_a)^2} \quad (\text{A.18})$$

where $\Theta_a = 2 \cdot (\theta_{wa}/b_{3a})$ and $\Delta_a = 2 \cdot (\delta_{wa}^*/b_{3a})$.

In the equations above the “momentum thickness” (θ_{wa}) and “displacement thickness” (δ_{wa}^*) are estimated using a procedure similar to that described for the volute (see Eq. (A.4)).

The entrance loss coefficient is to account for the abrupt area contraction loss applied to the meridional component of the velocity head:

$$Y_{ina} = \left[\left(\frac{A_{1a}}{A_{3a}} - 1 \right) \cdot \sin \alpha_{1a} \right]^2 \cdot \frac{(p_{01a} - p_{1a})}{(p_{03a} - p_{3a})} \quad (\text{A.19})$$

A.4. Rotor

The overall loss coefficient in the rotor has a different definition compared to the previous components:

$$Y_r = \frac{p_{03Rsr} - p_{03Rr}}{p_{03Rr} - p_{3r}} \quad (\text{A.20})$$

where $p_{03Rsr} = f(h_{03Rr}, s_{1r})$. It is estimated by calculating the following loss contributions: profile (Y_{pr}), incidence (Y_{incr}), blade loading (Y_{blr}), hub-to-shroud loading (Y_{hsr}), clearance (Y_{clr}):

$$Y_r = Y_{pr} + Y_{incr} + Y_{blr} + Y_{hsr} + Y_{clr} \quad (\text{A.21})$$

The profile loss is given by:

$$Y_{pr} = \frac{2 \cdot \Theta_r + \Delta_r^2}{(1 - \Delta_r)^2} \quad (\text{A.22})$$

where

$$\Theta_r = 1 - [1 - 2 \cdot (\theta_{wr}/b_{wr})] \cdot [1 - (\theta_{bsr}/b_{br} + \theta_{bpr}/b_{br})] \quad (\text{A.23})$$

$$\Delta_r = 1 - [1 - 2 \cdot \delta_{wr}^*/b_{wr}] \cdot [1 - (\delta_{bsr}^*/b_{br} + \delta_{bpr}^*/b_{br})] \quad (\text{A.24})$$

Like in the nozzle, three “momentum thicknesses” are defined to account for the flow condition at the wall, blade suction surface and blade pressure surface. The dimensional lengths used at the denominator are:

$$b_{br} = \text{esse}_{3r} \cdot \sin \beta_{3r} \quad (\text{A.25})$$

$$b_{wr} = b_{3r} \quad (\text{A.26})$$

The incidence loss is:

$$Y_{incr} = \sin^2(\alpha_{1r} - \alpha_{1r}^*) \cdot [p_{01r} - p_{1r}] / [p_{03r} - p_{3r}] \quad (\text{A.27})$$

where α_{1r}^* is the optimum rotor inlet flow angle. This loss is approximately null in this study because only design conditions are considered.

The blade loading loss is:

$$Y_{blr} = \frac{1}{24} \cdot \left[\frac{\Delta W}{W_{3r}} \right]^2 \quad (\text{A.28})$$

where ΔW is the relative velocity difference between suction and pressure surface which can be calculated by:

$$\Delta W = 4\pi \cdot |r_{3r} \cdot C_{t3r} - r_{1r} \cdot C_{t1r}| / (L_r \cdot N_r) \quad (\text{A.29})$$

The hub-to-shroud loading loss is:

$$Y_{hsr} = \frac{1}{6} \left(\frac{\kappa_m \cdot b_{3r} \cdot W_{2r}}{W_{3r} \cdot \sin \alpha_{3r}} \right)^2 \quad (\text{A.30})$$

where κ_m is the mean curvature of the meridional channel.

The blade clearance loss is:

$$Y_{clr} = \dot{m}_{CL} \cdot \Delta p / [\dot{m} \cdot (p_{03Rr} - p_{3r})] \quad (\text{A.31})$$

where \dot{m}_{CL} is the clearance gap leakage mass flow rate defined by:

$$\dot{m}_{cl} = \rho_{aver} \cdot u_{cl} \cdot L_r \cdot N_r \cdot \delta_c \quad (\text{A.32})$$

and δ_c is the clearance gap assumed equal to:

$$\delta_c = \max(0.0005; 0.015 \cdot b_{3r}) \quad (\text{A.33})$$

Finally the disk friction loss is given in terms of enthalpy drop by:

$$\Delta h_{df} = \frac{1}{2} \cdot \frac{C_M \cdot \rho_{aver} \cdot \omega^3 \cdot r_{1r}^5}{\dot{m}} \quad (\text{A.34})$$

where the torque coefficient (C_M) is calculated according to the approach by Daily and Nece [40]. Note that the disk friction losses are considered as external losses, so they do not influence the flow field inside the expander.

Appendix B. Design and performance results for two different working conditions

In this Section the values of the flow, thermodynamic and geometrical parameters obtained in the design and performance routines are shown in Tables B1–B3 for two scenarios which refer to subsonic (1) and supersonic (2) flow conditions at nozzle outlet. These two turbine designs use the same assumptions in terms of n_s and v_s to focus on the effect of VR on RIT geometry and performance. The corresponding expansion lines are also shown in h - s diagrams in Fig. B1.

References

- Pan L, Wang H. Improved analysis of Organic Rankine Cycle based on radial flow turbine. *Appl Therm Eng* 2013;61:606–15.
- Bahamonde S, Pini M, De Servi C, Rubino A, Colonna P. Method for the preliminary fluid dynamic design of high-temperature mini-ORC turbines. *J Eng Gas Turb Power* 2017. <http://dx.doi.org/10.1115/1.4035841>. [accepted manuscript. GTP-16-1517].
- Casati E, Vitale S, Pini M, Persico G, Colonna P. Centrifugal turbines for mini-organic rankine cycle power systems. *J Eng Gas Turb Power* 2014;136:122607.
- Ventura CAM, Jacobs PA, Rowlands AS, Petrie-Repar P, Sauret E. Preliminary design and performance estimation of radial inflow turbines: an automated approach. *J Fluid Eng-T ASME* 2012;134:031102.
- Wong CS, Krumdieck S. Scaling of gas turbine from air to refrigerants for organic rankine cycle using similarity concept. *J Eng Gas Turb Power* 2016;138:061701.
- Fiaschi D, Manfrida G, Maraschiello F. Thermo-fluid dynamics preliminary design of turbo-expanders for ORC cycles. *Appl Eng* 2012;97:601–8.
- Fiaschi D, Manfrida G, Maraschiello F. Design and performance prediction of radial ORC turboexpanders. *Appl Eng* 2015;138:517–32.
- Song J, Gu C-W, Ren X. Influence of the radial-inflow turbine efficiency prediction on the design and analysis of the Organic Rankine Cycle (ORC) system. *Energy Convers Manage* 2016;123:308–16.
- Rahbar K, Mahmoud S, Al-Dadah RK, Moazami N. Parametric analysis and optimization of a small-scale radial turbine for Organic Rankine Cycle. *Energy* 2015;83:696–711.
- Lang W, Colonna P, Almbauer R. Assessment of waste heat recovery from a heavy-duty truck engine by means of an ORC turbogenerator. *J Eng Gas Turb Power* 2013;135:042313.
- Whitfield A, Baines NC. Design of radial turbomachines. 1st ed. Harlow (England): Longman Scientific and Technical; 1990.
- Costall AW, Gonzalez Hernandez A, Newton PJ, Martinez-Botas RF. Design methodology for radial turbo expanders in mobile organic Rankine cycle applications. *Appl Eng* 2015;157:729–43.
- Fiaschi D, Innocenti G, Manfrida G, Maraschiello F. Design of micro radial turboexpanders for ORC power cycles: From 0D to 3D. *Appl Therm Eng* 2016;99:402–10.
- Sauret E, Gu Y. Three-dimensional off-design numerical analysis of an organic Rankine cycle radial-inflow turbine. *Appl Eng* 2014;135:202–11.
- Moustapha H, Zelesky MF, Baines NC, Japikse D. Axial and radial turbines. 1st ed. White River Junction: Concepts NREC; 2003.
- Baines NC. Radial turbines: an integrated design approach. In: 6th European turbomachinery conference – fluid dynamics and thermodynamics, Lille, France; 2005.
- Zheng Y, Hu D, Cao Y, Dai Y. Preliminary design and off-design performance analysis of an Organic Rankine Cycle radial-inflow turbine based on mathematic method and CFD method. *Appl Therm Eng* 2017;112:25–37.
- Li Y, Ren X-D. Investigation of the organic Rankine cycle (ORC) system and the radial-inflow turbine design. *Appl Therm Eng* 2016;96:547–54.
- Dong B, Xu G, Luo X, Zhuang L, Quan Y. Analysis of the supercritical organic Rankine cycle and the radial turbine design for high temperature applications. *Appl Therm Eng* 2017. <http://dx.doi.org/10.1016/j.applthermaleng.2016.12.123>.
- Al Jubori A, Daabo A, Al-Dadah RK, Mahmoud S, Ennil AB. Development of micro-scale axial and radial turbines for low-temperature heat source driven organic Rankine cycle. *Energy Convers Manage* 2016;130:141–55.
- Kang SH. Design and experimental study of ORC (organic Rankine cycle) and radial turbine using R245fa working fluid. *Energy* 2012;41:514–24.
- Kang SH. Design and preliminary tests of ORC (organic Rankine cycle) with two-stage radial turbine. *Energy* 2016;96:142–54.
- Guillaume L, Legros A, Desideri A, Lemort V. Performance of a radial-inflow turbine integrated in an ORC system and designed for a WHR on truck application: an experimental comparison between R245fa and R1233zd. *Appl Eng* 2017;186:408–22.
- Aungier RH. Turbine Aerodynamics: Axial-flow and radial-inflow turbine design and analysis. New York (USA): ASME Press; 2005.
- Macchi E, Perdichizzi A. Efficiency prediction for axial-flow turbines operating with nonconventional fluids. *J Eng Gas Turb Power* 1981;103:718–24.
- Angelino G, Gaia M, Macchi E. A review of Italian activity in the field of ORCs. In: Proc of the int VDI seminar, Zurich, CH; 1984.
- Perdichizzi A, Lozza G. Design criteria and efficiency prediction for radial inflow turbines. Anaheim, CA (USA): Proc of the gas turbine conf. and exhibition; 1987.
- Lazzaretto A, Manente G. A new criterion to optimize ORC design performance using efficiency correlations for axial and radial turbines. *Int J Thermodyn* 2014;17(3):173–81.
- Manente G, Da Lio L, Lazzaretto A. Influence of axial turbine efficiency maps on the performance of subcritical and supercritical Organic Rankine Cycle systems. *Energy* 2016;107:761–72.
- Lemmon EW, Huber ML, McLinden MO. NIST standard reference database 23: reference fluid thermodynamic and transport properties-REFPROP, version 9.1.
- Rohlik H. Analytical determination of radial inflow turbine design geometry for maximum efficiency. Tech rep TN D-4384. NASA, Lewis Research Center; 1975.
- Balje OE. Turbomachines: a guide to design, selection and theory. 1st ed. New York: John Wiley and Sons; 1981.
- Manente G. Analysis and development of innovative binary cycle power plants for geothermal and combined geo-solar thermal resources. Ph.D. thesis. Italy; University of Padova; 2011.
- Russell H, Rowlands A, Ventura C, Jahn I. Design and testing process for a 7 kW radial inflow refrigerant turbine at the University of Queensland. In: Proceedings of ASME turbo expo 2016, Seoul, South Korea; 2016 [paper no GT2016-58111].
- Li YS, Lu GL. Radial turbine and centrifugal compressor. Beijing: China Machine Press; 1987.
- Dixon SL, Hall CA. Fluid Mechanics and Thermodynamics of Turbomachinery. 6th ed. Burlington: Butterworth Heinemann; 2010.
- Suhrmann JF, Peitsch D, Gugau M, Heuer T, Tomm U. Validation and development of loss models for small size radial turbines. In: Proceedings of ASME turbo expo, Glasgow, UK; 2010 [paper no GT2010-22666].
- Da Lio L, Manente G, Lazzaretto A. New efficiency charts for the optimum design of axial flow turbines for organic Rankine cycles. *Energy* 2014;77:447–59.
- Da Lio L, Manente G, Lazzaretto A. Predicting the optimum design of single stage axial expanders in ORC systems: is there a single efficiency map for different working fluids? *Appl Eng* 2016;167:44–58.
- Daily JW, Nece RE. Chamber dimensions effects on induced flow and frictional resistance of enclosed rotating disks. *J Basic Eng* 1960;82:217–32.